Inorg. Chem. **2007**, *46*, 8193–8207

Metal–Porphyrin Orbital Interactions in Highly Saddled Low-Spin Iron(III) Porphyrin Complexes

Yoshiki Ohgo,[†,‡] Akito Hoshino,[§] Tomoya Okamura,[†] Hidehiro Uekusa,[||] Daisuke Hashizume,[¶] Akira Ikezaki,[†] and Mikio Nakamura*[,†,‡,§]

Department of Chemistry, School of Medicine, Toho University, Ota-ku, Tokyo 143-8540, Japan, Research Center for Materials with Integrated Properties, Toho University, Funabashi 274-8510, Japan, Division of Chemistry, Graduate School of Science, Toho University, Funabashi 274-8510, Japan, Graduate School of Science and Engineering, Tokyo Institute of Technology, Tokyo 152-8551, Japan, and Molecular Characterization Team, RIKEN, Wako, 351-0198, Japan

Received April 30, 2007

Substituent effects of the *meso*-aryl (Ar) groups on the ^{1}H and ^{13}C NMR chemical shifts in a series of low-spin highly saddled iron(III) octaethyltetraarylporphyrinates, [Fe(OETArP)L_2]$^+$, where axial ligands (L) are imidazole (HIm) and *tert*-butylisocyanide (^{t}BuNC), have been examined to reveal the nature of the interactions between metal and porphyrin orbitals. As for the bis(HIm) complexes, the crystal and molecular structures have been determined by X-ray crystallography. These complexes have shown a nearly pure saddled structure in the crystal, which is further confirmed by the normal-coordinate structural decomposition method. The substituent effects on the CH_2 proton as well as meso and CH_2 carbon shifts are fairly small in the bis(HIm) complexes. Since these complexes adopt the $(d_{xy})^2(d_{xz}, d_{yz})^3$ ground state as revealed by the electron paramagnetic resonance (EPR) spectra, the unpaired electron in one of the metal d_π orbitals is delocalized to the porphyrin ring by the interactions with the porphyrin $3e_g$-like orbitals. A fairly small substituent effect is understandable because the $3e_g$-like orbitals have zero coefficients at the *meso*-carbon atoms. In contrast, a sizable substituent effect is observed when the axial HIm is replaced by ^{t}BuNC. The Hammett plots exhibit a large negative slope, –220 ppm, for the *meso*-carbon signals as compared with the corresponding value, +5.4 ppm, in the bis(HIm) complexes. Since the bis(^{t}BuNC) complexes adopt the $(d_{xz}, d_{yz})^4(d_{xy})^1$ ground state as revealed by the EPR spectra, the result strongly indicates that the half-filled d_{xy} orbital interacts with the specific porphyrin orbitals that have large coefficients on the *meso*-carbon atoms. Thus, we have concluded that the major metal–porphyrin orbital interaction in low-spin saddle-shaped complexes with the $(d_{xz}, d_{yz})^4(d_{xy})^1$ ground state should take place between the d_{xy} and a_{2u}-like orbital rather than between the d_{xy} and a_{1u}-like orbital, though the latter interaction is symmetry-allowed in saddled D_{2d} complexes. Fairly weak spin delocalization to the *meso*-carbon atoms in the complexes with electron-withdrawing groups is then ascribed to the decrease in spin population in the d_{xy} orbital due to a smaller energy gap between the d_{xy} and d_π orbitals. In fact, the energy levels of the d_{xy} and d_π orbitals are completely reversed in the complex carrying a strongly electron-withdrawing substituent, the 3,5-bis(trifluoromethyl)phenyl group, which results in the formation of the low-spin complex with an unprecedented $(d_{xy})^2(d_{xz}, d_{yz})^3$ ground state despite the coordination of ^{t}BuNC.

Introduction

Interactions between metal and porphyrin orbitals are important factors that can determine the physicochemical properties of naturally occurring heme proteins as well as synthetic model heme complexes.[1–8] Among the porphyrin π orbitals, either an a_{1u} or a_{2u} orbital is considered to be the highest-occupied molecular orbital (HOMO) in porphyrins with D_{4h} symmetry.[3–5] Because these orbitals are orthogonal

* To whom correspondence should be addressed. E-mail: mnakamu@med.toho-u.ac.jp.
† School of Medicine, Toho University.
‡ Research Center for Materials with Integrated Properties, Toho University.
§ Graduate School of Science, Toho University.
|| Tokyo Institute of Technology.
¶ RIKEN.

(1) *Physical Method in Bioinorganic Chemistry*; Que, L., Jr., Ed.; University Science Books, Sausalito, CA, 2000.
(2) *Inorganic Electronic Structure and Spectroscopy*; Solomon, E. I., Lever, A. B. P., Eds.; John Wiley & Sons, Inc.: New York, 1999; Vol. 1.

10.1021/ic700827w CCC: $37.00
Published on Web 08/29/2007

Chart 1. Symmetry Presentation of Metal and Porphyrin Orbitals in Metal Porphyrinates[a]

Metal	D_{4h} planar	D_{2d} ruffle	D_{2d} Saddle
$d_{x^2-y^2}$	b_{1g}	b_1	b_2
d_{z^2}	a_{1g}	a_1	a_1
d_{xz}, d_{yz}	e_g	e	e
d_{xy}	b_{2g}	b_2	b_1
Porphyrin			
LUMO	e_g	e	e
HOMO	a_{1u}	b_1	b_1
	a_{2u}	b_2	b_2
HOMO-1	e_g	e	e

[a] Adapted from refs 9 and 10.

to any of the iron d orbitals, no interactions can be expected between the a_{1u} or a_{2u} orbitals and iron d orbitals. Actually, however, the metal porphyrin complexes usually have lower symmetry because of (i) the presence of peripheral substituents, (ii) the orientation of planar axial ligands such as pyridine or imidazole, and (iii) the deformation of the normally planar porphyrin ring. Thus, it is possible that the porphyrin HOMO, which is originally classified as either a_{1u} or a_{2u} in D_{4h} complexes, is involved in the interactions with iron d orbital(s) in various metal porphyrinates. Chart 1 lists the symmetry representations of the metal d and porphyrin frontier orbitals in metal porphyrinates with planar D_{4h}, ruffled D_{2d}, and saddled D_{2d} structures.[9,10] As shown in Chart 1, the metal d_π (d_{xz} and d_{yz}) orbitals can interact with one of the porphyrin π orbitals, HOMO-1, regardless of the deformation mode of the porphyrin ring since these orbitals have the same symmetry in D_{4h} and D_{2d} complexes. If we confine the metal porphyrinates to the low-spin iron(III) complexes, the d_{xy} orbital could interact with the a_{2u}-like orbital in ruffled complexes and with the a_{1u}-like orbital in saddled complexes;[9,10] we use hereafter the symmetry labels such as a_{1u}-like or a_{2u}-like in the ruffled and saddled complexes, although they should be signified as either b_1 or b_2 in deformed complexes as shown in Chart 1. Other symmetry-allowed interaction should take place between the $d_{x^2-y^2}$ and a_{1u}-like orbitals in ruffled complexes and between the $d_{x^2-y^2}$ and a_{2u}-like orbitals in saddled complexes.[9−12] However, these interactions must be less important because the $d_{x^2-y^2}$ orbital is vacant and is located far above the occupied d_{xy}, d_{xz}, and d_{yz} orbitals in six-coordinate low-spin iron(III) complexes. In Chart 2, the frontier orbitals of D_{4h} porphyrin are given.

Chart 2. Frontier Orbitals of Porphyrin

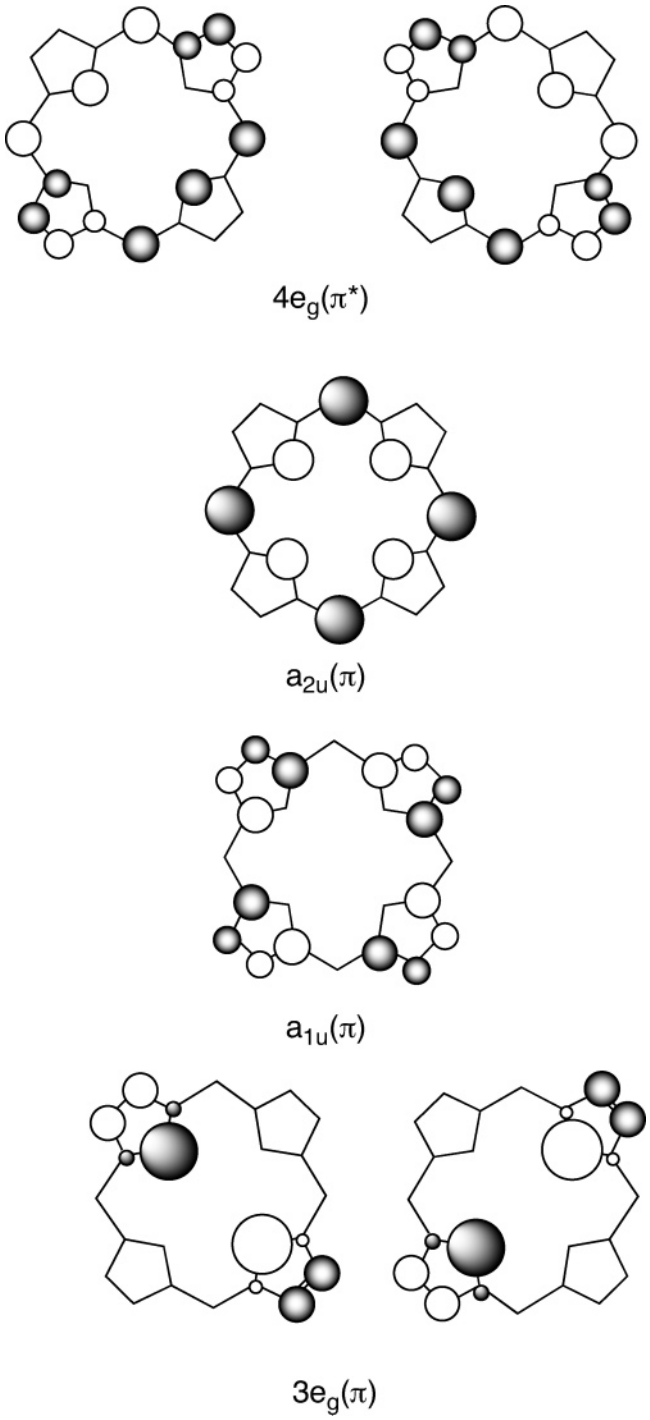

There are ample examples showing the presence of the $d_{xy}-a_{2u}$ interaction in low-spin ruffled complexes.[3−5,13−21] The

(3) Walker, F. A. In *The Porphyrin Handbook*, Kadish, K. M., Smith, K. M., Guilard, R., Eds.; Academic Press, San Diego, CA, 2000; Vol. 5, Chapter 36, pp 81−183.
(4) Walker, F. A.; Simonis, U. In *Biological Magnetic Resonance*; Berrliner, L. J., Reuben, J., Eds.; Plenum Press, New York, 1993; Vol. 12, pp 133−273.
(5) Walker, F. A. *Chem. Rev.* **2004**, *104*, 589−616.
(6) Nakamura, M. *Coord. Chem. Review.* **2006**, *250*, 2271−2294.
(7) Goff, H. M. *Nuclear Magnetic Resonance of Iron Porphyrins.* In *Iron Porphyrins, I*; Lever, A. B. P., Gray, H. B., Eds.; Physical Bioinorganic Chemistry Series 1; Addison-Wesley: Reading, MA, 1983; pp 237−281.
(8) Bertini, I.; Luchinat, C. In *NMR of Paramagnetic Substances*; Lever, A. B. P., Ed.; Coordination Chemistry Reviews 150; Elsevier: Amsterdam, The Netherlands, 1996; pp 29−75.
(9) Cheng, R.-J.; Chen, P.-Y.; Lovell, T.; Liu, T.; Noodleman, L.; Case, D. A. *J. Am. Chem. Soc.* **2003**, *125*, 6774−6783.
(10) Cjonradie, J.; Ghosh, A. *J. Phys. Chem. B* **2003**, *107*, 6486−6490.
(11) Ghosh, A.; Harvorsen, I.; Nilsen, H. J.; Steene, E.; Wondimagegn, T.; Lie, R.; Caemelbecke, E. van; Guuo, N.; Ou, Z.; Kadish, K. M. *J. Phys. Chem. B* **2001**, *105*, 8120−8124.
(12) Shao, J.; Steene, E.; Hoffman, B. M.; Ghosh, A. *Eur. J. Inorg. Chem.* **2005**, 1609−1615.

Chart 3

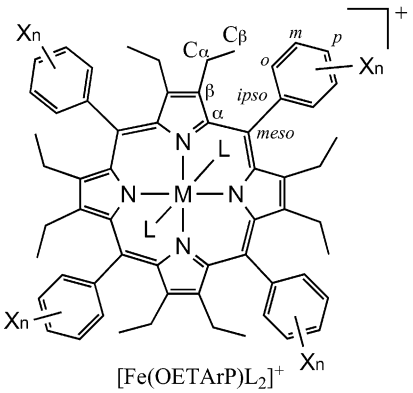

[Fe(OETArP)L$_2$]$^+$	
Ar = Substituted phenyl	
4-CH_3O-	(**1$_a$**, **1$_b$**)
H-	(**2$_a$**, **2$_b$**)
4-CF_3-	(**3$_a$**, **3$_b$**)
2,6-Cl_2-	(**4$_a$**, **4$_b$**)
3,5-$(CF_3)_2$-	(**5$_a$**, **5$_b$**)
Axial Ligand (L)	
L = HIm(**a**)	
L = ^{t}BuNC(**b**)	

[Zn(OETArP)]	
Ar = Substituted phenyl	
4-CH_3O-	(**1$_{Zn}$**)
H-	(**2$_{Zn}$**)
4-CF_3-	(**3$_{Zn}$**)
2,6-Cl_2-	(**4$_{Zn}$**)
3,5-$(CF_3)_2$-	(**5$_{Zn}$**)

relevance of this interaction to the biological process was recently pointed out by Rivera and co-workers in the metabolism of heme oxygenase.[22,23] In contrast, the $d_{xy}-a_{1u}$ interaction in low-spin saddled complexes is rarely reported. Quite recently, Cheng and co-workers suggested on the basis of the DFT calculation that the saddle-shaped intermediate-spin complex, $[Fe(OETPP)(THF)_2]^+$, should adopt the $(d_{xz}, d_{yz})^3(d_{xy})^1(d_z^2)^1$ electron configuration.[24] This is because the $d_{xy}-a_{1u}$ interaction is strong enough to lift the d_{xy} orbital above the d_{xz} and d_{yz} orbitals. Since this conclusion is against our original proposal that $[Fe(OETPP)(THF)_2]^+$ should adopt the $(d_{xy})^2(d_{xz}, d_{yz})^2(d_z^2)^1$ electron configuration,[25,26] we have reexamined how the $d_{xy}-a_{1u}$ interaction affects the electronic structure of saddle-shaped iron(III) porphyrinates. To begin, the effect of the $d_{xy}-a_{1u}$ interaction on the electronic structure of low-spin saddled complexes has been examined on the basis of the ^{1}H and ^{13}C NMR chemical shifts as well as electron paramagnetic resonance (EPR) *g* values. Thus, we have prepared a series of low-spin complexes [Fe(OETArP)-$L_2]^+$ (**1$_{a,b}$**−**5$_{a,b}$**) (OETArP = octaethyltetraarylporphyrinates), where Ar represents various substituted phenyl groups and the axial ligand (L) is either imidazole (HIm, **a**) or *tert*-butylisocyanide (^{t}BuNC, **b**) as shown in Chart 3. We have also prepared the corresponding diamagnetic Zn(OETArP) complexes (**1$_{Zn}$**−**5$_{Zn}$**) to estimate the isotropic shifts of some ^{1}H and ^{13}C signals of **1$_{a,b}$**−**5$_{a,b}$**. The molecular structures of some of the bis(imidazole) complexes, **1$_a$**−**4$_a$**, have been determined by X-ray crystallography.

Results

Structures of [Fe(OETArP)(HIm)$_2$]$^+$. 1. Crystal Packing. Crystal packing diagrams of **1$_a$**−**4$_a$** are given in Figures S1−S4 of the Supporting Information, respectively. The crystals of **1$_a$** and **3$_a$** are isomorphic; the crystal system is monoclinic, and the space group is $P2_1$ in both complexes, as listed in Table 1. Each molecule in **1$_a$** and **3$_a$** is connected with the neighboring molecules by the hydrogen bonding between HIm and ClO_4^-. As a result, chiral molecular helices represented by (N7)HIm−Fe−HIm(N8)···(O3)ClO_4(O2)···(N7*)HIm*−Fe*−HIm*(N8*)···(O3*)ClO_4(O2*) develop along the *b* axis, where * means the symmetry transformation along the *b* axis (symmetry code: $x, 1 + y, z$). It should be noted that chiral crystals are formed due to the chiral arrangement of the molecules, though the molecules of **1$_a$** and **3$_a$** are essentially achiral. Thus, the recrystallization batch contains the same amount of chiral helices with opposite helicities, but in a certain single crystal either one of opposite helices should exist, exclusively.

The crystal of **2$_a$** contains eight chloroform molecules and one cyclohexane molecule. The cyclohexane molecule is on the center of symmetry in the asymmetric unit. Two chloroform molecules are highly disordered. One of the imidazole ligands is connected to the Cl anion by hydrogen bonding, and the same anion is further connected with the imidazole ligand of the neighboring complex by hydrogen bonding. Thus, the one-dimensional hydrogen-bonding network represented by (N6)HIm−Fe−HIm(N8)···Cl···(N6*)-HIm*−Fe*−HIm*(N8*)···Cl* develops along the *a* axis, where * means the symmetry transformation along the *a* axis (symmetry code: $1 + x, y, z$). It should be noted that the Cl

(13) Safo, M. K.; Walker, F. A.; Raitsimring, A. M.; Walters, W. P.; Dolata, D. P.; Debrunner, P. G.; Scheidt, W. R. *J. Am. Chem. Soc.* **1994**, *116*, 7760−7770.
(14) Nakamura, M.; Ikeue, T.; Fujii, H.; Yoshimura, T. *J. Am. Chem. Soc.* **1997**, *119*, 6284−6291.
(15) Wolowiec, S.; Latos-Grazynski, L.; Mazzanti, M.; Marchon, J.-C. *Inorg. Chem.* **1997**, *36*, 5761−5771.
(16) Wojaczynski, J.; Latos-Grazynski, L.; Glowiak, T. *Inorg. Chem.* **1997**, *36*, 6299−6306.
(17) Pilard, M.-A.; Guillemot, M.; Toupet, L.; Jordanov, J.; Simonneaux, G. *Inorg. Chem.* **1997**, *36*, 6307−6314.
(18) Wolowiec, S.; Latos-Grazynski, L.; Toronto, D.; Marchon, J.-C. *Inorg. Chem.* **1998**, *37*, 724−732.
(19) Mazzanti, M.; Marchon, J.-C.; Wojaczynski, J.; Wolowiec, S.; Latos-Grazynski, L.; Shang, M.; Scheidt, W. R. *Inorg. Chem.* **1998**, *37*, 2476−2481.
(20) Veyrat, M.; Ramasseul, R.; Turowska-Tyrk, I.; Scheidt, W. R.; Autret, M.; Kadish, K. M.; Marchon, J.-C. *Inorg. Chem.* **1999**, *38*, 1772−1779.
(21) Ikeue, T.; Ohgo, Y.; Saitoh, T.; Nakamura, M.; Fujii, H.; Yokoyama, M. *J. Am. Chem. Soc.* **2000**, *122*, 4068−4076.
(22) Caignan, G. A.; Deshmukh, R.; Zeng, Y.; Wilks, A.; Bunce, R. A.; Rivera, M. *J. Am. Chem. Soc.* **2003**, *125*, 11842−11852.
(23) Rivera, M.; Caignan, G. A.; Astashkin, A. V.; Raitsimring, A. M.; Shokhireva, T. K.; Walker, F. A. *J. Am. Chem. Soc.* **2002**, *124*, 6077−6089.
(24) Cheng, R.-J.; Wang, Y.-K.; Chen, P.-Y.; Han Y.-P.; Chang, C.-C. *Chem. Commun.* **2005**, 1312−1314.
(25) Sakai, T.; Ohgo, Y.; Ikeue, T.; Takahashi, M.; Takeda, M.; Nakamura, M. *J. Am. Chem. Soc.* **2003**, *125*, 13028−13029.
(26) Hoshino, A.; Ohgo, Y.; Nakamura, M. *Inorg. Chem.* **2005**, *44*, 7333−7344.

Table 1. Crystal Data of a Series of Imidzole Complexes

	[Fe(4-OMe-OETPP-(HIm)$_2$]C1O$_4$ **1$_a$**	[Fe(OETPP)-(HIm)$_2$]C1 **2$_a$**	[Fe(4-CF3-OETPP-(HIm)$_2$]C1O$_4$ **3$_a$**	[Fe(2,6-C1$_2$-OETPP)-(HIm)$_2$]C1O$_4$ **4$_a$**
chemical formula	$C_{70}H_{76}N_8O_8FeCl\cdot(CH_2Cl_2)$	$C_{66}H_{68}N_8FeC1\cdot(C_6H_{12})_{0.5}\cdot(CHC1_3)_4$	$C_{701}H_{64}N_8O_4F_{12}$-FeCl$\cdot(CH_2Cl_2)$	$C_{66}H_{60}N_8O_4FeCl_9\cdot(C_6H_6)_{0.5}\cdot(CH_2Cl_2)$
cryst dimens (mm)	0.51 × 0.40 × 0.12	0.2 × 0.1 × 0.1	0.2 × 0.2 × 0.1	0.2 × 0.2 × 0.1
cryst color	purple	purple	purple	purple
cryst syst	monoclinic	triclinic	monoclinic	triclinic
space group	$P2_1$ (No. 4)	$P\bar{1}$ (No. 2)	$P2_1$ (No. 4)	$P\bar{1}$ (No. 2)
M_r	1333.61	1584.13	1485.52	1528.10
a (Å)	13.082(1)	12.412(1)	12.918(2)	11.816(4)
b (Å)	18.000(2)	13.784(1)	18.784(3)	14.594(5)
c (Å)	15.531(2)	24.500(1)	15.434(2)	22.483(7)
α (deg)	90	74.439(3)	90	76.480(15)
β (deg)	112.151(1)	82.914(1)	110.509(6)	83.346(14)
γ (deg)	90	81.725(3)	90	71.053(12)
V (Å^3)	3387.3(6)	3980.0(5)	3507.7(9)	3562(2)
Z	2	2	2	2
D_x (Mg m^{-3})	1.308	1.322	1.406	1.425
T (K)	90	298	298	298
diffractometer	Rigaku VariMax	Rigaku RAXIS-RAPID	Rigaku RAXIS-RAPID	Rigaku RAXIS-RAPID
abs corr	numerical (T_{min} = 0.865, T_{max} = 0.964)	multiscan (T_{min} = 0.865, T_{max} = 0.934)	multiscan (T_{min} = 0.918, T_{max} = 0.959)	multiscan (T_{min} = 0.880, T_{max} = 0.941)
$2\theta_{max}$ (deg)	65.1	55.0	55.0	55.0
limiting indices	$-18 < h < 18$ $-25 < k < 20$ $-16 < l < 21$	$-16 < h < 16$ $-17 < k < 17$ $-31 < l < 31$	$-16 < h < 16$ $-22 < k < 24$ $-20 < l < 20$	$-15 < h < 15$ $-18 < k < 18$ $-28 < l < 29$
no. of indep reflns	17 672	17 686	15 115	15 816
no. of reflns with $>2\sigma(I)$	13 714	10 384	13 216	13 129
no. of params	859	993	926	863
R_{int}	0.0366	0.0650	0.0456	0.0351
R1	0.0538	0.0959	0.0607	0.0756
wR2	0.1300	0.2640	0.1685	0.2169
S	1.016	1.010	1.097	1.087
$(\Delta/\sigma)_{max}$	<0.001	<0.001	<0.001	<0.001

anion, which bridges two iron(III) porphyrinates, is further involved in the hydrogen bonding with the three chloroform molecules.

In the crystal of **4$_a$**, the perchlorate oxygen atoms bind two molecules by hydrogen bonding to form a one-dimensional hydrogen-bonding network along the *b* axis, which is represented as (N8)HIm−Fe−HIm(N6)···(O3)-ClO4(O1)···N(8*)HIm*−Fe*−HIm*(N7*)···(O3*)ClO4-(O1*), where * means the symmetry transformation along the *b* axis (symmetry code: x, $1 + y$, z).

2. Molecular Structures. The molecular structures of **1$_a$**−**4$_a$** are given in Figure 1 and Figures S5−S7 of the Supporting Information, respectively. The displacement of each atom of the porphyrin core from the 24-atom mean plane is shown in Figure 2. Table 2 lists the structural parameters of these complexes together with those of some analogous complexes reported previously.[27−30] Various structural parameters listed in Table 2 are defined as follows: ϕ is the orientation angle of the axial ligand to the nearest N_P-Fe-N_P axis, θ is the dihedral angle between two axial ligands, τ is the dihedral angle between the average N4 plane and each pyrrole ring, ψ is the dihedral angle between two diagonal pyrrole rings, η is the twist angle between two diagonal pyrrole rings, ω is the dihedral angle between phenyl group and the $C_\alpha-C_{meso}-C_{\alpha'}$ plane, and $|\Delta C_{meso}|$ and $|\Delta C_\beta|$ are the average deviation of the *meso*- and β-pyrrole carbon atoms from the mean porphyrin plane, respectively.[29] Table 3 lists the results of the normal-coordinate structural decomposition (NSD) method, which reveals the distortion modes of the complexes more quantitatively.[31−33] Figure 2 and the data in Table 3 clearly indicate that all the bis(Him) complexes examined in this study commonly exhibit highly saddled structures, though some structural differences have been observed among complexes. The average deviations of the β-pyrrole carbon atoms from the mean porphyrin plane are 1.15−1.26 Å. These values are close to the corresponding values in analogous $[Fe(OETPP)(DMAP)_2]^+$ and $[Fe(OETPP)-(Py)_2]^+$.[27−29] The average deviations of the *meso*-carbon atoms are 0.04−0.10 Å. Thus, each complex includes a small ruffling in a highly saddled porphyrin core. The NSD result given in Table 3 shows the deformation mode of these complexes more quantitatively.[31−33] The B_{2u} (saddle) coefficient ranges from 3.4809 to 3.7849 and is tremendously greater than any other coefficients. In fact, the ratio of the

(27) Ogura, H.; Yatsunyk, L.; Medforth, C. J.; Smith, K. M.; Barkigia, K. M.; Renner, M. W.; Melamed, D.; Walker, F. A. *J. Am. Chem. Soc*. **2001**, *123*, 6564−6578.
(28) Ohgo, Y.; Ikeue, T.; Nakamura, M. *Inorg. Chem.* **2002**, *41*, 1698−1700.
(29) Ohgo, Y.; Ikeue, T.; Takahashi, M.; Takeda, M.; Nakamura, M. *Eur. J. Inorg. Chem.* **2004**, 798−809.
(30) Yatsunyk, L. A.; Dawson, A.; Carducci, M. D.; Nichol, G. S.; Walker, F. A. *Inorg. Chem*. **2006**, *45*, 5417−5428.
(31) Shelnutt, J. A.; Song, X.-Z.; Ma, J.-G.; Jia, S.-L.; Jentzen, W.; Medforth, C. J. *Chem. Soc. Rev.* **1998**, *27*, 31−41.
(32) Jentzen, W.; Song, X.-Z.; Shelnutt, J. A. *J. Phys. Chem. B* **1997**, *101*, 1684−1699.
(33) Jentzen, W.; Ma, J.-G.; Shelnutt, J. A. *Biophys. J.* **1998**, *74*, 753−763.

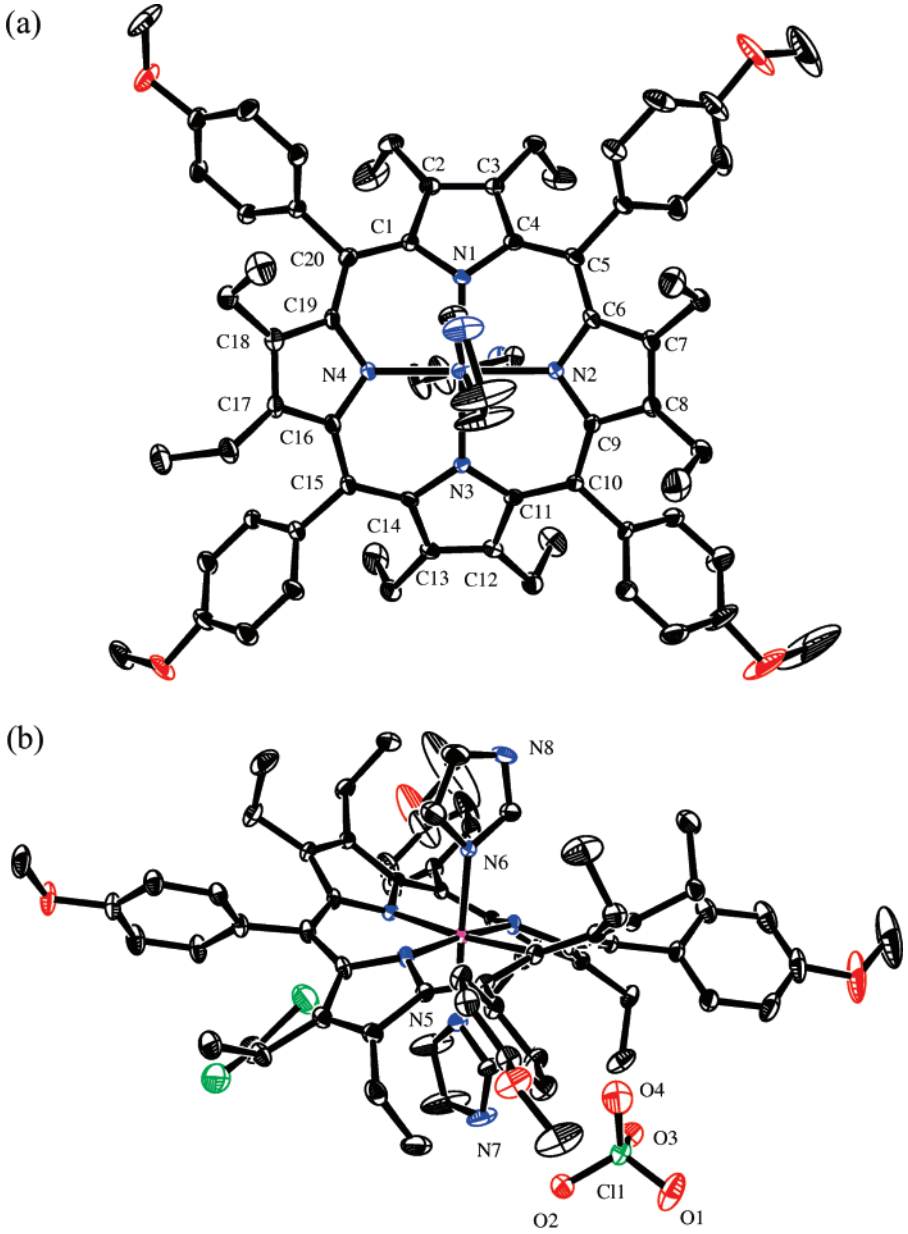

Figure 1. ORTEP diagrams of $\mathbf{1_a}$ together with the atom labeling: (a) top view; (b) side view. Thermal ellipsoids are drawn at the 50% probability level.

saddled deformation reaches as great a value as 95%. As expected from the small deviation of the *meso*-carbons from the mean porphyrin plane, the ratio of the ruffled deformation is at most 6%. Thus, we can say that these complexes have nearly pure saddled structure in the crystal. It should be noted here that $\mathbf{2_a}$ has a relatively large A_{2u} (dome) coefficient. The result can be ascribed to the unique crystal packing of this complex; one of the imidazole ligands rotates about the Fe−N(HIm) bond and deviates from the Fe−N(pyrrole) axis for the formation of hydrogen bonding with the Cl anion. As a result, the steric environment around this ligand is more congested than that of the other ligand. Correspondingly, the average displacement of the β-carbons at the crowded side decreases to 1.08 Å as compared with 1.23 Å in the less-crowded opposite side. It is this curious deviation that increases the A_{2u} (dome) coefficient.

Although two axial ligands are perpendicularly aligned in $\mathbf{1_a}$ and $\mathbf{3_a}$ as revealed from $\theta = 88.2°$ and 87.4°, respectively, the θ values have decreased to 73.3° and 46.4° in $\mathbf{4_a}$ and $\mathbf{2_a}$, respectively. As mentioned, the fairly small dihedral angle in $\mathbf{2_a}$ has been ascribed to the deviation of one of the imidazole ligands from the Fe−N(pyrrole) axis to form the hydrogen bond with the Cl anion. Since imidazole is a less-bulky ligand as compared with other aromatic ligands such as pyridine, the imidazole ligand can easily rotate around the Fe−N(imidazole) bond and deviate from the Fe−N(pyrrole) axis to the position that is favorable for effective packing. This must be one of the reasons why the structural parameters such as ϕ and θ are different among a series of $[Fe(OETArP)(HIm)_2]^+$ complexes examined in this study.

The ratios of the average bond lengths, $Fe-N_{axial}/Fe-N_p$, in $\mathbf{1_a}-\mathbf{4_a}$ are quite close to unity; they are 0.998, 0.998, 1.004, and 1.007, respectively. The result indicates that the coordination geometry around the iron center is nearly octahedral. In contrast, the corresponding ratios in analogous $[Fe(OETPP)(DMAP)_2]^+$ and $[Fe(OETPP)(Py)_2]^+$ are much

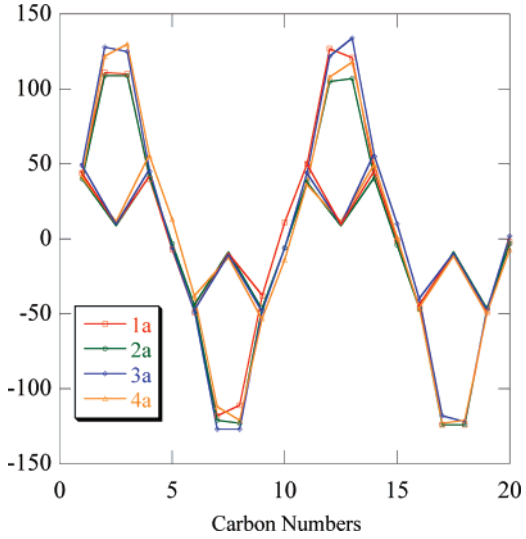

Figure 2. Vertical displacement of the peripheral atoms.

larger, 1.025 and 1.109 at 298 K, respectively. The shorter Fe−N_{axial} bonds in $\mathbf{1_a}$−$\mathbf{4_a}$ as compared with those of the bis(DMAP) and bis(Py) complexes are the indication that the ligand field of HIm is much stronger than that of DMAP and Py. Neither the Fe−N_P nor the Fe−N_{axial} bond has exhibited appreciable change depending on the *p*-substituents. It should be noted here that the structural parameters of **2a** obtained in this study are somehow different from those reported by Yatsunyk and co-workers.[30] The discrepancies should be ascribed to the differences in crystal system and space group between these two crystals; the crystal system and the space group reported by Yatsunyk and co-workers are trigonal and $P3_221$, respectively.[30]

Close inspection of the molecular structures given in Figure 1 and Figures S5−S7 (Supporting Information) reveals that the relative orientation of the eight ethyl groups is quite different among the four complexes. Since the stable conformation of an ethyl group attached to the *β*-carbon of the pyrrole ring is the one where the $\beta-C_\alpha-C_\beta$ (see Chart 3) plane is nearly perpendicular to the pyrrole plane, there should be two possible orientations in an ethyl group, *u* (or up) and *d* (or down), depending on the positions of the ethyl group relative to the average porphyrin plane. Figures S5 and S6 (Supporting Information) clearly indicate that the eight ethyl groups of $\mathbf{2_a}$ and $\mathbf{3_a}$ exhibit the commonly observed *uuddduud* orientation, though one of the ethyl groups in $\mathbf{2_a}$ is disordered to take both the *u* and *d* orientations. The same orientation of the peripheral ethyl groups is observed in $[Fe(OETPP)(2\text{-}MeIm)_2]^+$,[27] $[Fe(OETPP)(DMAP)_2]^+$,[29] $[Fe(OETPP)(Ph)]^+$,[34] $[Fe(OETPP)(1\text{-}MeIm)_2]^+$,[35] $[Fe(OETPP)(4\text{-}CNPy)_2]^+$,[36] and Fe(OETPP)Cl.[37] In contrast, the ethyl groups of $\mathbf{1_a}$ show a *uudduuud* orientation where one of the pyrrole rings has oppositely

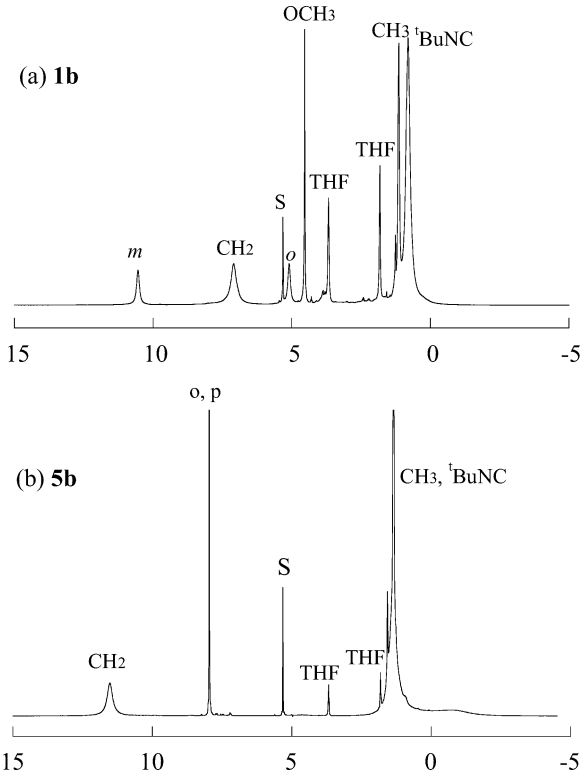

Figure 3. ^{1}H NMR spectra of (a) $\mathbf{1_b}$ and (b) $\mathbf{5_b}$ taken in CD_2Cl_2 solution at 298 K.

directing ethyl groups. This orientation is also a commonly observed one. Complexes such as $[Fe(OETPP)(DMAP)_2]^+$,[27] $[Fe(OETPP)(Py)_2]^+$,[28] $[Fe(OETPP)(4\text{-}CNPy)_2]^+$,[36] and Fe(OETPP)$ClO_4$[38] take the same orientation. In the case of $\mathbf{4_a}$, the ethyl groups take the *ududdduud* orientation, where any of the two ethyl groups in the same pyrrole ring take the opposite orientation probably because of the severe steric repulsion with the bulky chloro groups.

^{1}H NMR Chemical Shifts. ^{1}H NMR spectra of $\mathbf{1_b}$ and $\mathbf{5_b}$ taken in CD_2Cl_2 solution at 298 K are shown in Figure 3 as typical examples. Table 4 lists the chemical shifts of a series of low-spin $[Fe(OETArP)(HIm)_2]^+$ ($\mathbf{1_a}$−$\mathbf{5_a}$) and $[Fe(OETArP)(^tBuNC)_2]^+$ ($\mathbf{1_b}$−$\mathbf{5_b}$) determined at 298 K together with the Hammett *σ* values. The chemical shifts of some diamagnetic Zn(OETArP) ($\mathbf{1_{Zn}}$−$\mathbf{5_{Zn}}$) are also listed to estimate the isotropic shifts.[39] The chemical shifts of the CH_2 signals of $\mathbf{1_a}$−$\mathbf{5_a}$ given in Table 4a are extrapolated values from low temperature since these signals are very broad at 298 K due to the inversion of the saddled porphyrin ring. In parentheses in Table 4a are given the chemical shifts at 223 K where the CH_2 protons give separated signals. The chemical shifts of the CH_2 signals of $\mathbf{1_b}$−$\mathbf{5_b}$ given in Table 4b are the average values of two diastereotopic CH_2 signals. This is because the CH_2 protons of $\mathbf{1_b}$−$\mathbf{5_b}$ exhibit quite sharp signals at 298 K; they have given two signals only when the temperature is lower than 223 K.[40] In the parentheses of

(34) Bill, E.; Schunemann, V.; Trautwein, A. X.; Weiss, R.; Fischer, J.; Tabard, A.; Guilard, R. *Inorg. Chem. Acta* **2002**, *339*, 420−426.
(35) Yatsunyk, L. A.; Carducci, M. D.; Walker, F. A. *J. Am. Chem.* Soc. **2003**, *125*, 15986−16005.
(36) Yatsunyk, L. A.; Walker, F. A. *Inorg. Chem.* **2004**, *43*, 757−777.
(37) Cheng, R.-J.; Chen, P.-Y.; Gau, P.-R.; Chen, C.-C.; Peng, S.-M. *J. Am. Chem. Soc.* **1997**, *119*, 2563−2569.
(38) Barkigia, K. M.; Renner, M. W.; Fajer, F. *J. Porphyrins Phthalocyanines* **2001**, *5*, 415−418.
(39) Hoshino, A.; Ohgo, Y.; Nakamura, M. *Tetrahedron Lett.* **2005**, *46*, 4961−4964.
(40) Ikeue, T.; Ohgo, Y.; Saitoh, T.; Yamaguchi, T.; Nakamura, M. *Inorg. Chem.* **2001**, *40*, 3423−3434.

Table 2. Comparison of Structural Parameters for $[Fe(OETPP)L_2]^+$

complexes	*T*/*K*	Fe−N_p/Å	Fe−N_{axial}/Å	ϕ/deg	θ/deg	τ/deg	ψ/deg	η/deg	ω/deg	$\lvert\Delta C_{meso}\rvert$/0.01 Å	$\lvert\Delta C_\beta\rvert$/0.01 Å	cavity/Å^3
$\mathbf{1_a}$	90	1.979(2)	1.975(3)	14.6(3) 16.6(3)	88.2(2)	30.2(8)	119.6(1)	2.5(3)	65.4(2)	6	118	14.64
$\mathbf{2_a}$	298	1.975(3)	1.972(3)	11.6(5) 31.8(4)	46.4(3)	29.5(1)	121.0(1)	0.4(4)	64.9(3)	4	115	26.70
$\mathbf{2_a}$[a]	170	1.980(4)	1.936(9) 1.998(7)	11.1(4) −19.0(2)	30.1(4)				46.7(2)	20	113	
$\mathbf{2_a}$[a]	170	1.961(4)	1.962(7) 1.973(9)	12.1(5) 17.7(5)	57.2(5)				46.1(2)	19	114	
$\mathbf{3_a}$	298	1.971(3)	1.979(3)	4.0(4) 0.4(4)	87.4(2)	32.3(1)	115.5(1)	2.0(4)	62.4(2)	6	126	17.62
$\mathbf{4_a}$	298	1.966(3)	1.980(3)	5.4(4) 21.8(4)	73.3(2)	30.2(2)	119.6(2)	5.2(3)	67.7(3)	10	120	22.95
[Fe(OETPP)-(DMAP)$_2$]$^+$ [b]	298	1.977(2)	2.030(3)	10.6(2) 25.0(2)	53.2	30.8(1)	118.4(1)	4.0(2)	66.7(2)	8	122	
[Fe(OETPP)-(DMAP)$_2$]$^+$ [c]	298	1.951	2.000	9 29	70	33[e]	114[e]	17[e]	66	28	122	
$[Fe(OETPP)Py_2]^+$ [d]	298	1.985	2.201	1.1(4) 3.6(3)	82.3	32.4(1)	115.2(2)	1.2(3)	40.6(1)	3	124	28.88 32.08
$[Fe(OETPP)Py_2]^+$ [d]	80	1.957	1.993	6.3(3) 11.6(3)	85.1	30.8(1)	118.5(1)	3.0(3)	64.5(3)	6	121	23.19

[a] Yatsunyk, L. A. et al.[30] [b] Ohgo, Y. et al.[29] [c] Ogura, H. et al.[27] [d] Ohgo, Y. et al.[28] [e] These angles are calculated on the basis of the structural data reported by Ogura et al.[27]

Table 3. NSD of Distortion Modes of Complexes

complexes	D_{oop}	B_{2u}, saddle	B_{1u}, ruffle	A_{2u}, dome	$E_{g(x)}$, wave (*x*)	$E_{g(y)}$, wave (*y*)	A_{1u}, propeller	sum	sad/sum	ruf/sum
$\mathbf{1_a}$	3.5796	3.5796	0.1175	0.0255	0.0700	0.0446	0.0007	3.8379	0.93	0.03
$\mathbf{2_a}$	3.4837	3.4809	0.0206	0.1341	0.0174	0.0244	0.0068	3.6842	0.95	<0.01
$\mathbf{3_a}$	3.7921	3.7894	0.0716	0.0427	0.0401	0.1084	0.0184	4.0706	0.93	0.02
$\mathbf{4_a}$	3.6392	3.6298	0.2432	0.0322	0.0714	0.0285	0.0477	4.0528	0.90	0.06

Table 4. ^{1}H NMR Chemical Shifts in CD_2Cl_2 Solutions at 298 K. (a) $[Fe(OETArP)(HIm)_2]^+$, (b) $[Fe(OETArP)(^tBuNC)_2]^+$, and (c) [Zn(OETArP)] Chemical Shifts in Parentheses in (a) and (b) Are Determined at 223 and 193 K, Respectively

complexes	$\Sigma\sigma$	CH_2	CH_2 (avg)	CH_3	ortho	meta	para	^{t}Bu
			(a) $[Fe(OETArP)(HIm)_2]^+$					
$\mathbf{1_a}$	−0.27	4.74, 10.98[a]	7.86[a]	0.74	5.64	5.49	3.35[b]	
		(3.69, 12.45)	(8.07)	(1.39)	(3.02)	(4.36)	(2.73[b])	
$\mathbf{2_a}$	0.00	4.37, 10.34[a]	7.34	0.86	4.97	5.8	6.73	
		(3.22, 11.81)	(7.52)	(1.28)	(2.76)	(4.68)	(5.99)	
$\mathbf{3_a}$	0.54	4.32, 10.69[a]	7.51	0.92	4.90	6.00		
		(3.06, 12.20)	(7.40)	(1.39)	(2.62)	(4.83)		
$\mathbf{4_a}$		5.54, 9.71[a]	7.63	1.18		5.42	6.32	
		(4.76, 10.62)	(7.69)	(1.72)		(4.09)	(5.45)	
$\mathbf{5_a}$	0.86	3.56, 10.91[a]	7.24	1.05	5.23		1.17	
		(2.09, 12.72)	(7.41)	(1.32)	(3.04)		(6.38)	
			(b) $[Fe(OETArP)(^tBuNC)_2]^+$					
$\mathbf{1_b}$	−0.27	7.10	7.10	1.14	5.10	10.55		−1.55[a]
		(5.1, 18.0)	(11.6)	(1.67)	(6.49)	(10.95)		(−4.57)
$\mathbf{2_b}$	0.00	7.46	7.46	1.32	5.54	11.05	6.31	−1.53[a]
		(5.7, 18.4)	(11.9)	(1.63)	(6.68)	(11.40)	(6.80)	(−4.06)
$\mathbf{3_b}$	0.54	9.93	9.93	1.27	7.00	10.14		−1.03[a]
		(7.4, 24.8)	(16.1)	(1.86)	(8.43)	(9.75)		(−3.28)
$\mathbf{4_b}$		12.39	12.39	1.73		9.35	7.53	−1.03[a]
		(8.8, 20.8)	(14.8)	(2.09)		(10.97)	(7.43)	(−2.15)
$\mathbf{5_b}$	0.86	10.83	10.83	1.36	7.96		7.96	−0.95[a]
		(8.0, 30.2)	(19.1)	(1.95)	(8.94)		(8.47)	(−1.78)
				(c) Zn(OETArP)				
$\mathbf{1_{Zn}}$	−0.27	2.10, 2.65	2.38	0.45	8.19	7.24	4.07[b]	
$\mathbf{2_{Zn}}$	0.00	2.01, 2.61	2.31	0.46	8.31	7.67	7.79	
$\mathbf{3_{Zn}}$	0.54	1.97, 2.63	2.30	0.49	8.52	8.03		
$\mathbf{4_{Zn}}$		2.45	2.45	0.71		7.76	7.65	
$\mathbf{5_{Zn}}$	0.86	1.52	1.52	1.26	8.87		8.36	

[a] Extrapolated values; signals are too broad at ambient temperature. [b] Methoxy signal.

Table 4b are given the chemical shifts determined at 193 K where the CH_2 protons give separated signals. As shown in Figure 3, the coordinated and free ^{t}BuNC protons showed a broad single line at 298 K due to the fast ligand exchange on the ^{1}H NMR time scale. However, the signal started to split into two signals below 273 K. Thus, the chemical shifts at 298 K are the extrapolated values from low temperature where the free and coordinated ^{t}BuNC give different signals.

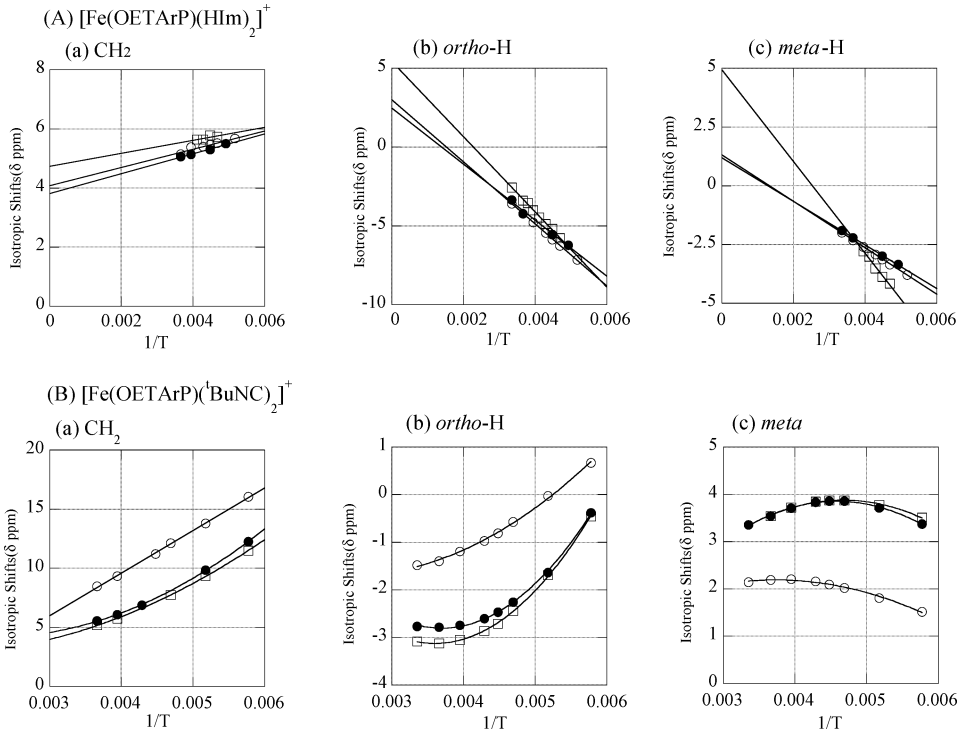

Figure 4. Curie plots of the isotropic shifts of (a) CH_2, (b) *o*-H, and (c) *m*-H signals of (A) $[Fe(OETArP)(HIm)_2]^+$ ($\mathbf{1_a}-\mathbf{3_a}$) and (B) $[Fe(OETArP)(^t BuNC)_2]^+$ ($\mathbf{1_b}-\mathbf{3_b}$) taken in CD_2Cl_2 solutions. Complexes **1**−**3** are signified by squares, filled circles, and open circles, respectively.

Figure 4 shows the Curie plots of the CH_2, *o*-H, and *m*-H signals of $\mathbf{1_a}-\mathbf{3_a}$ and $\mathbf{1_b}-\mathbf{3_b}$, where the isotropic shifts (δ_{iso}) are plotted against $1/T$. The isotropic shifts of some selected ^1H signals were determined by $\delta_{iso} = \delta_{obs} - \delta_{dia}$. δ_{obs} is the chemical shift of a ^1H signal in paramagnetic $[Fe(OETArP)L_2]^+$ and δ_{dia} is the chemical shift of the corresponding signal in diamagnetic Zn(OETArP). Curie plots for each proton signal of $\mathbf{1_a}-\mathbf{3_a}$ given in Figure 4A showed a straight line in the temperature range examined, though the isotropic shifts at $1/T = 0$ deviated by at most 5 ppm. While the slopes of the Curie plots for the CH_2 signals were positive, those for the *o*-H and *m*-H signals were negative. In contrast, the Curie plots for each proton signal of $\mathbf{1_b}-\mathbf{3_b}$ given in Figure 4B exhibited a considerable curvature in the temperature range examined.

^{13}C NMR Chemical Shifts. The ^{13}C NMR spectra of $\mathbf{1_b}$ and $\mathbf{5_b}$ taken in CD_2Cl_2 solution at 298 K are shown in Figure 5 as typical examples. Table 5 lists the ^{13}C NMR chemical shifts of a series of low-spin $[Fe(OETArP)(HIm)_2]^+$ ($\mathbf{1_a}-\mathbf{5_a}$) and $[Fe(OETArP)(^tBuNC)_2]^+$ ($\mathbf{1_b}-\mathbf{5_b}$) complexes determined at 298 K. The ^{13}C NMR chemical shifts of a series of diamagnetic $\mathbf{1_{Zn}}-\mathbf{4_{Zn}}$ complexes are also listed; the ^{13}C NMR chemical shifts of $\mathbf{5_{Zn}}$ were not determined due to its fairly low solubility. In the case of $[Fe(OETArP)(HIm)_2]^+$ and Zn(OETArP), the assignment of the α and β signals was hampered due to their close proximity. Thus, the chemical shifts of these signals signified by asterisks in Table 5 could be reversed.

Hammett Plots of the ^{1}H and ^{13}C NMR Isotropic Shifts. The isotropic shifts of some selected signals of $[Fe(OETArP)(HIm)_2]^+$ ($\mathbf{1_a}-\mathbf{3_a}$ and $\mathbf{5_a}$) and $[Fe(OETArP)(^tBuNC)_2]^+$ ($\mathbf{1_b}-\mathbf{3_b}$ and $\mathbf{5_b}$) were plotted against Hammett σ values by the red and blue lines, respectively, as shown in Figure 6. We could not determine the isotropic shifts of the carbon signals of $\mathbf{5_a}$ and $\mathbf{5_b}$, since the ^{13}C NMR chemical shifts of diamagnetic $\mathbf{5_{Zn}}$ were unavailable due to its low solubility. Thus, we estimated the isotropic shifts of these carbon signals in $\mathbf{5_a}$ and $\mathbf{5_b}$ by assuming that the ^{13}C chemical shifts of $\mathbf{5_{Zn}}$ are the same as those of $\mathbf{3_{Zn}}$. Figure 6 clearly indicates that both the isotropic shifts and the slopes of the Hammett plots are very different between the bis(HIm) and

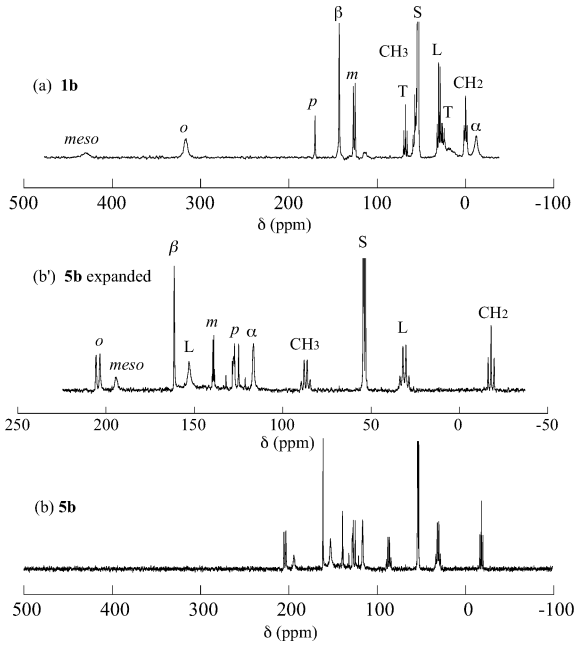

Figure 5. ^{13}C NMR spectra of (a) $\mathbf{1_b}$ and (b) $\mathbf{5_b}$ taken in CD_2Cl_2 solution at 298 K.

Table 5. ^{13}C NMR Chemical Shifts of (a) $[Fe(OETArP)(HIm)_2]^+$, (b) $[Fe(OETArP)(^tBuNC)_2]^+$, and (c) Zn(OETArP) Taken in CD_2Cl_2 Solutions at 298 K

complexes	meso	α	β	ortho	meta	para	ipso	C_α	C_β
				(a) $[Fe(OETArP)(HIm)_2]^+$					
$\mathbf{1_a}$	−2	182[a]	179[a]	102	111	156	163	−23	91
$\mathbf{2_a}$	7	162[a]	167*	107	124	125	162	−24	87
$\mathbf{3_a}$	5	157[a]	166[a]	108	122		166	−24	86
$\mathbf{4_a}$	−7	149[a]	161[a]	113	128	128	154	−27	92
$\mathbf{5_a}$	6	144[a]	164[a]	109	128	119	161	−25	85
				(b) $[Fe(OETArP)(^tBuNC)_2]^+$					
$\mathbf{1_b}$	430	−11	143	317	126	171	n.d.	0	58
$\mathbf{2_b}$	417	−5	143	310	144	138	37	−2	59
$\mathbf{3_b}$	280	79	152	244	135	n.d.	98	−10	75
$\mathbf{4_b}$	166	136	157	205	133	133	125	−21	93
$\mathbf{5_b}$	194	117	161	207	139	126	128	−18	87
				(c) Zn(OETArP)					
$\mathbf{1_{Zn}}$	119	148[a]	144[a]	135	113	160	135	19.9	17.5
$\mathbf{2_{Zn}}$	119	147[a]	144[a]	136	127	128	142	19.8	17.5
$\mathbf{3_{Zn}}$	118	147[a]	144[a]	136	124	131	145	20.0	17.4
$\mathbf{4_{Zn}}$	113	147[a]	144[a]	141	129	131	139	20.0	16.1
$\mathbf{5_{Zn}}$				too broad to detect					

[a] The assignments of the α and β signals could be reversed.

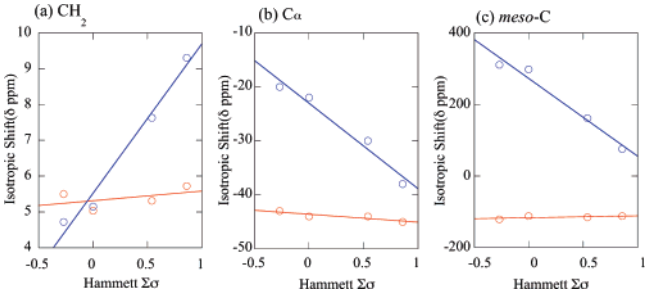

Figure 6. Hammett plots of the ^1H and ^{13}C NMR isotropic shifts of bis(HIm) complexes ($\mathbf{1_a}$−$\mathbf{3_a}$ and $\mathbf{5_a}$, red), and bis(^{t}BuNC) complexes ($\mathbf{1_b}$−$\mathbf{3_b}$ and $\mathbf{5_b}$, blue): (a) CH_2−H, (b) C_α, and (c) *meso*-C.

bis(^{t}BuNC) complexes. The slopes of the CH_2, C_α, and *meso*-C lines in $[Fe(OETArP)(HIm)_2]^+$ are 0.27, −1.4, and +5.4 ppm, respectively, while those in $[Fe(OETArP)(^t$-$BuNC)_2]^+$ are +4.2, −16, and −220 ppm, respectively.

EPR *g* Values. The EPR spectra taken in frozen CH_2Cl_2 or CH_2Cl_2/toluene solution at 4−20 K are given in Figure 7. The EPR spectra of both $\mathbf{2_a}$ and $\mathbf{2_b}$ are omitted since they have already been reported in our previous paper.[40] Figures S8(A)−S8(D) of the Supporting Information show the simulated spectra. The *g* values thus obtained are listed in Table 6. In the case of $[Fe(OETArP)(HIm)_2]^+$, all the complexes except $\mathbf{4_a}$ exhibited rhombic-type spectra; $\mathbf{4_a}$ showed a so-called large g_{max}-type spectrum. In the case of $[Fe(OETArP)(^tBuNC)_2]^+$, all the complexes except $\mathbf{5_b}$ showed axial-type spectra. It is quite unusual that $\mathbf{5_b}$ exhibited the rhombic-type spectrum despite the coordination of ^{t}BuNC. Figure 8 demonstrates the energy gap between the d_{xy} and d_π orbitals of $[Fe(OETArP)(^tBuNC)_2]^+$ determined on the basis of the EPR *g* values.[41−44] In each complex, the average

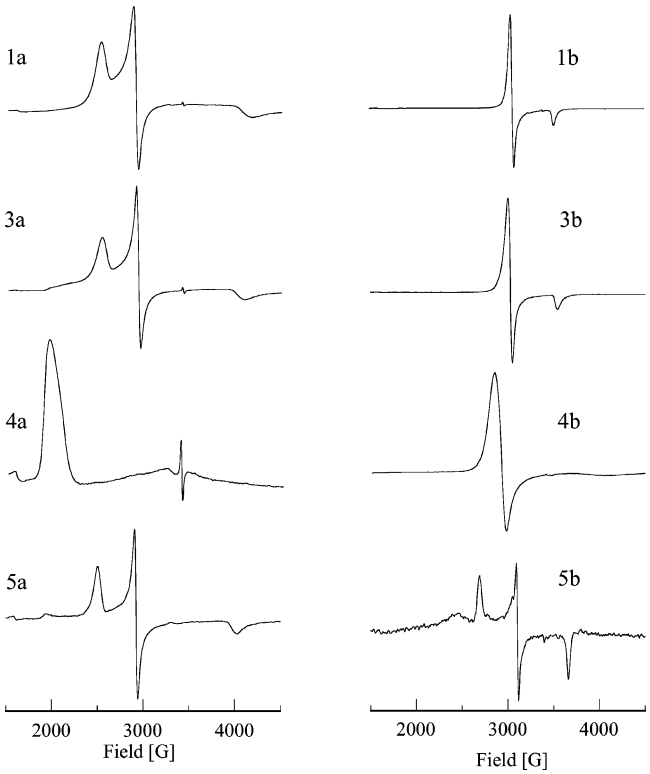

Figure 7. EPR spectra of bis(HIm) complexes ($\mathbf{1_a}$ and $\mathbf{3_a}$−$\mathbf{5_a}$) and bis(^{t}-BuNC) complexes ($\mathbf{1_b}$ and $\mathbf{3_b}$−$\mathbf{5_b}$) taken in frozen CH_2CH_2 solution at 4.2−20 K.

Table 6. EPR *g* Values of $[Fe(OETArP)(HIm)_2]^+$ and $[Fe(OETArP)(^tBuNC)_2]^+$ Taken in Frozen CH_2Cl_2 Solution at 4.2−20 K

complexes	g_1	g_2	g_3	complexes	g_1	g_2	g_3
$\mathbf{1_a}$	2.73	2.36	1.65	$\mathbf{1_b}$	2.216		1.925
$\mathbf{2_a}$	2.72	2.37	1.64	$\mathbf{2_b}$	2.29	2.25	1.92
$\mathbf{3_a}$	2.71	2.36	1.66	$\mathbf{3_b}$	2.250		1.908
$\mathbf{4_a}$	3.45			$\mathbf{4_b}$	2.370		1.680
$\mathbf{5_a}$	2.73	2.34	1.69	$\mathbf{5_b}$	2.524	2.186	1.859

values of the energy levels of the three d orbital are fixed at a constant value.

Molecular Orbital Calculation. The energy levels of some important molecular orbitals in a series of Zn(OETArP) complexes ($\mathbf{1_{Zn}}$−$\mathbf{4_{Zn}}$) have been determined by DFT calculation. As the *p*-substituent changes from OMe ($\mathbf{1_{Zn}}$) to H ($\mathbf{2_{Zn}}$), and then to CF_3 ($\mathbf{3_{Zn}}$), both the HOMO and lowest unoccupied molecular orbital (LUMO) are gradually stabilized, as shown in Figure S9 of the Supporting Information. In the case of $\mathbf{4_{Zn}}$ (2,6-Cl_2), both the HOMO and LUMO are located between those of $\mathbf{2_{Zn}}$ and $\mathbf{3_{Zn}}$ despite the presence of two electron-withdrawing chloro substituents at the 2,6-positions.

Discussion

General Considerations about the Effects of meso Substituents on the Heme Electronic Structure. The electronic ground state of low-spin iron(III) porphyrinates can most directly be determined by EPR spectroscopy. Complexes that adopt the $(d_{xy})^2(d_{xz}, d_{yz})^3$ ground state exhibit either the rhombic or large g_{max}-type spectra depending on the orientation of planar axial ligands; the complexes with parallel aligned axial ligands show the rhombic-type spectra while those with perpendicularly aligned axial ligands show

(41) Walker, F. A. *Coord. Chem. Rev.* **1999**, *185*−*186*, 471−534.
(42) Palmer, G. *Electron Paramagnetic Resonance of Hemoproteins*. In *Iron Porphyrins, Part II;* Lever, A. B. P., Gray, H. B., Eds.; Physical Bioinorganic Chemistry Series 2; Addison-Wesley: Reading, MA, 1983; pp 43−88.
(43) Bohan, T. L. *J. Magn. Reson.* **1977**, *22*, 109−118.
(44) Taylor, C. P. S. *Biochim. Biophys. Acta* **1977**, *491*, 137−149.

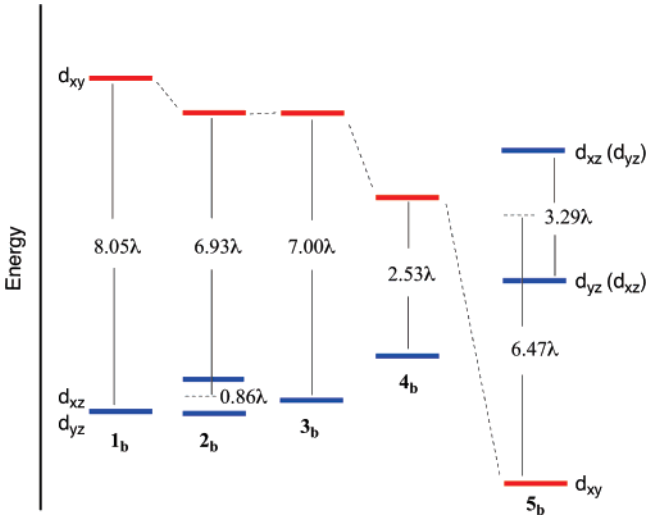

Figure 8. Relative energy levels of the d_{xy}, d_{xz}, and d_{yz} orbitals of bis(^{t}BuNC) complexes (**1$_b$**−**5$_b$**) obtained on the basis of the EPR g values in frozen CH_2Cl_2 solution at 4.2−20 K where λ is a spin−orbit coupling constant. In each complex, the average value of the energy levels of three d orbitals is fixed at a constant value.

the large g_{max}-type spectra.[30,35,45,46] In contrast, the complexes that adopt the $(d_{xz}, d_{yz})^4(d_{xy})^1$ ground state always exhibit the axial-type spectra.[3,40]

While the EPR method is used for the determination of the heme electronic ground state at extremely low temperatures, the NMR method is available at much higher temperatures.[1−8] The ^{1}H and ^{13}C NMR chemical shifts of low-spin iron(III) porphyrinates are composed of the contact and dipolar terms. In the case of the planar D_{4h} complexes with the $(d_{xy})^2(d_{xz}, d_{yz})^3$ ground state, the d_π(d_{xz} or d_{yz}) orbital carrying an unpaired electron can interact with the filled $3e_g$ orbitals and to a lesser extent with the vacant $4e_g$* orbitals of porphyrin.[3−6] Thus, the unpaired electron in the d_π orbital delocalizes to the porphyrin ring, especially to the pyrrole β carbons since the $3e_g$ orbital has relatively large coefficient at these positions. As mentioned, the d_π−$3e_g$ type interaction is possible not only in the planar D_{4h} but also in the six-coordinate ruffled and saddled D_{2d} complexes because both the d_π and $3e_g$ orbitals are represented as e symmetry, as shown in Chart 1. Thus, the $[Fe(OETArP)(L)_2]^{\pm}$ complexes with the $(d_{xy})^2(d_{xz}, d_{yz})^3$ ground state should induce the downfield shift of the CH_2 signals and upfield shift of the C_α signals.[26] Furthermore, the ^{1}H and ^{13}C chemical shifts must be insensitive to the *meso*-phenyl substituents since the $3e_g$ orbital has a zero coefficient at the *meso*-carbon atoms, as shown in Chart 2.

In the complexes with the $(d_{xz}, d_{yz})^4(d_{xy})^1$ ground state, the d_{xy} orbital carrying an unpaired electron is orthogonal to any of the porphyrin π orbitals in the D_{4h} complexes. Thus, there should be no spin delocalization to the peripheral carbon atoms. Actually however, the low-spin iron(III) porphyrinates with the $(d_{xz}, d_{yz})^4(d_{xy})^1$ ground state commonly exhibit the highly ruffled structure.[47−49] This is because the complex can be stabilized by the interaction between the half-filled d_{xy} orbital and the filled a_{2u} orbital by ruffling the porphyrin core. Since the a_{2u} orbital has a large coefficient at the meso position, the interaction induces not only a large downfield shift but also a large substituent effect to the *meso*-carbon signals.

Another symmetry-allowed interaction in low-spin iron(III) complexes should be the d_{xy}−a_{1u} interaction in the saddled D_{2d} complexes, as recently pointed out by Cheng and co-workers.[24] As revealed by the EPR and NMR studies, the low-spin iron(III) porphyrinates having ^{t}BuNC as axial ligand always exhibit the $(d_{xz}, d_{yz})^4(d_{xy})^1$ ground state regardless of the structure of the porphyrin cores. This is because the low-lying π* orbitals of ^{t}BuNC stabilize the d_π orbitals of iron(III) to the point that is lower than the d_{xy} orbital.[3−6] In fact, highly saddled $[Fe(OETPP)(^tBuNC)_2]^+$ (**2b**) is well characterized to adopt the $(d_{xz}, d_{yz})^4(d_{xy})^1$ ground state on the basis of the EPR, ^{1}H NMR, and ^{13}C NMR spectroscopy.[40,50] It is then expected that the ^{1}H and ^{13}C NMR chemical shifts of a series of saddled complexes could reveal which porphyrin orbital interacts with the half-occupied d_{xy} orbital. If the d_{xy}−a_{1u} interaction is the major interaction in these complexes, the effect of the *meso*-aryl substituent on the ^{1}H and ^{13}C chemical shifts must be quite small. Furthermore, the *meso*-carbon signal should appear at an extremely upfield position. This is because the a_{1u} orbital has large coefficient at the α and zero coefficient at the *meso*-carbon atoms as shown in Chart 2. If, on the contrary, the d_{xy}−a_{2u} interaction is the major interaction because of some contribution of the ruffled deformation in solution, the *meso*-carbon signal should appear at an extremely downfield position. In addition, the substituent effects on the *meso*-carbon and *meso*-aryl proton shifts must be much larger because the *meso*-carbons have large coefficients in the a_{2u} orbital, as shown in Chart 2. Thus, the substituent effect on the chemical shifts can tell the nature of the metal−porphyrin orbital interaction.

Orbital Interactions in Low-Spin $[Fe(OETArP)(HIm)_2]^+$ Complexes. Low-spin bis(imidazole) complexes usually adopt the $(d_{xy})^2(d_{xz}, d_{yz})^3$ ground state. In fact, we have already reported that highly saddled $[Fe(OETPP)(HIm)_2]^+$ adopts the $(d_{xy})^2(d_{xz}, d_{yz})^3$ ground state on the basis of the EPR and NMR results.[40] The EPR spectra given in Figure 7 clearly indicate that all the complexes examined in this study adopt the $(d_{xy})^2(d_{xz}, d_{yz})^3$ ground state at least at extremely low temperatures because these complexes exhibited either rhombic (**1a**−**3a** and **5a**) or large g_{max}-type (**4a**) spectra. However, the EPR spectral types observed here were against our expectation. As proposed by Walker and co-workers, EPR spectral type is closely connected with dihedral angles, θ, between two

(45) Walker, F. A.; Reis, D.; Balke, V. L. *J. Am. Chem. Soc.* **1984**, *106*, 6888−6898.
(46) Walker, F. A.; Huynh, B. H.; Scheidt, W. R.; Osvath, S. R. *J. Am. Chem. Soc.* **1986**, *108*, 5288−5297.
(47) Scheidt, W. R. In *The Porphyrin Handbook*; Kadish, K. M., Smith, K. M., Guilard, R., Eds.; Academic Press: San Diego, CA, 2000; Vol. 3, Chapter 16, pp 49−112.
(48) Walker, F. A.; Nasri, H.; Turowska-Tyrk, I.; Mohanrao, K.; Watson, C. T.; Shokhirev, N. V.; Debrunner, P. G.; Scheidt, W. R. *J. Am. Chem. Soc.* **1996**, *118*, 12109−12118.
(49) Simonneaux, G.; Schünemann, V.; Morice, C.; Carel, L.; Toupet, L.; Winkler, H.; Trautwein, A. X.; Walker, F. A. *J. Am. Chem. Soc.* **2000**, *122*, 4366−4377.
(50) Yatsunyk, L. A.; Walker, F. A. *Inorg. Chem.* **2004**, *43*, 4341−4352.

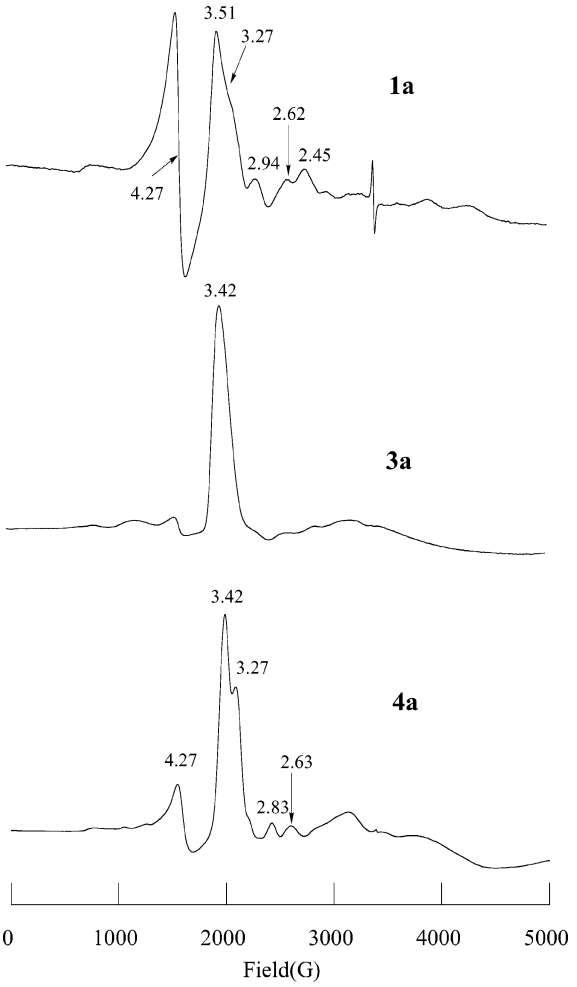

Figure 9. EPR spectra of bis(HIm) complexes (**1a**, **3a**, and **4a**) taken in the solid at 4.2 K.

planar axial ligands such as imidazole and pyridine.[30,35,45,46] Thus, EPR spectrum changes from rhombic to large g_{max}-type if θ becomes larger than ca. 57°.[30] In fact, **2a** with a dihedral angle of 46.4° showed a rhombic spectrum and **4a** with a dihedral angle of 73.2° showed a large g_{max}-type spectrum. In the case of **1a** and **3a**, however, the observed EPR spectra are rhombic, though the dihedral angles of these complexes are larger than 57°; they are 88.2° and 87.4°, respectively. The discrepancies should be ascribed to the difference in dihedral angles between solution and solid; the dihedral angles in **1a** and **3a** in solution could be much smaller than 57°. To ascertain if this is the case, we have measured the EPR spectra of **1a**, **3a**, and **4a** at 4.2 K in the solid and given them in Figure 9. Although **1a** and **4a** showed a signal at $g = 4.3$ probably due to the contamination of the monoadduct, all of these complexes commonly exhibited strong large g_{max}-type signals at $g = 3.3-3.5$ together with several minor peaks classified as rhombic-type signals. Thus, the results obtained from the solid samples are consistent with the general rule proposed by Walker and co-workers.[30] As mentioned, only **4a** exhibits the large g_{max}-type spectrum both in solution and in the solid. The results should be ascribed to the presence of bulky 2,6-chloro groups near the ligand, which could prohibit the flexibility of the ligand molecules and maintain the dihedral angle in the solid even in solution.

To reveal the electronic ground state at ambient temperature, we have examined the ^{1}H and ^{13}C NMR chemical shifts. The ^{1}H NMR data listed in Table 4 indicate that the CH_2 signals appear at δ 7.2−7.9 ppm as compared with 1.5−2.5 ppm in diamagnetic [Zn(OETArP)]. The ^{13}C NMR data listed in Table 5 indicate that the C_α signals appear at δ −23 to −27 ppm, which are by 43−47 ppm more upfield than those of the corresponding diamagnetic [Zn(OETArP)]. The *meso*-C signals are also observed upfield, at δ −7 to +7 ppm, as compared with δ 113−119 ppm in diamagnetic [Zn(OETArP)]. The downfield shift of the CH_2 signals and the upfield shift of the C_α signals are the direct indication that the pyrrole β carbons have sizable amounts of positive spin, which in turn indicates that all of these complexes adopt the $(d_{xy})^2(d_{xz}, d_{yz})^3$ ground state at 298−198 K; the unpaired electron in the d_π orbital delocalizes to the porphyrin ring especially on the β-carbon atoms due to the interactions between iron d_π and porphyrin $3e_g$-like orbitals. The large upfield shift of the meso signal also support this electronic structure since the $3e_g$ orbital has a zero coefficient at the *meso*-carbon positions; the *meso*-C signal shifts upfield if the spin density of the *meso*-carbons is negligibly small and that of the neighboring α-carbons is fairly large.[6,51]

The isotropic shifts of some selected ^{1}H and ^{13}C signals of $[Fe(OETArP)(HIm)_2]^+$ (**1a**−**3a** and **5a**) were plotted against Hammett σ values, as shown by the red lines in Figure 6. The slope of the Hammett plots of CH_2 signals in Figure 6a is +0.27 ppm. The results indicate that the substituent effects on the CH_2 chemical shifts are fairly small. The Hammett plots of the C_α and *meso*-C signals are given in parts b and c of Figure 6, respectively. The slopes of these lines are again fairly small; they are −1.4 and +5.4 ppm, respectively. The results indicate that all the low-spin $[Fe(OETArP)(HIm)_2]^+$ complexes examined in this study adopt the $(d_{xy})^2(d_{xz}, d_{yz})^3$ ground state even at ambient temperatures and that the major interaction affecting the chemical shifts occurs between the half-filled iron d_π and filled porphyrin $3e_g$-like orbitals.

Orbital Interactions in Low-Spin [Fe(OETArP)(^{t}BuNC)$_2$]$^+$ Complexes. As mentioned, low-spin bis(^{t}BuNC) iron(III) porphyrinates always adopt the $(d_{xz}, d_{yz})^4(d_{xy})^1$ ground state regardless of the type of porphyrins.[40] In fact, the EPR spectra of all the complexes except $\mathbf{5_b}$ are axial, which clearly indicate that they adopt the $(d_{xz}, d_{yz})^4(d_{xy})^1$ ground state at extremely low temperatures. We happened to find that $\mathbf{5_b}$ is actually the first bis(^{t}BuNC) complex of iron(III) porphyrinate that shows the $(d_{xy})^2(d_{xz}, d_{yz})^3$ ground state. If we expand the range from porphyrins to porphyrinoids, diazaporphyrin iron(III) complex [Fe(DAzP)(^{t}BuNC)$_2$]$^+$ is the first example that shows the $(d_{xy})^2(d_{xz}, d_{yz})^3$ ground state.[52]

(51) Rivera, M.; Caignan, G. A. *Anal. Bioanal. Chem.* **2004**, *378*, 1464−1483.
(52) Ohgo, Y.; Neya, S.; Uekusa, H.; Nakamura, M. *Chem. Commun.* **2006**, 4590−4592.

In contrast to the case of $[Fe(OETArP)(HIm)_2]^+$, most of the ^1H and ^{13}C signals in $[Fe(OETArP)(^tBuNC)_2]^+$ exhibited considerable substituent dependence, as revealed from the data in Tables 4 and 5. The Hammett plots of some ^1H and ^{13}C signals of $\mathbf{1_b}-\mathbf{3_b}$ and $\mathbf{5_b}$ are also given in Figure 6 by the blue lines for comparison with those of $[Fe(OETArP)(HIm)_2]^+$. For each signal, the substituent effect on the chemical shifts is considerably much larger in $[Fe(OETArP)(^tBuNC)_2]^+$ than in $[Fe(OETArP)(HIm)_2]^+$. The isotropic shift of the CH_2 signal has increased from +4.72 to +9.31 ppm with the increase in Hammett σ value as shown in Figure 6a. Correspondingly, the isotropic shift of the C_α signal has decreased from −20 to −38 ppm as shown in Figure 6b. The isotropic shift of the *meso*-C signal has also decreased from 311 to 76 ppm as shown in Figure 6c on going from $\mathbf{1_b}$ to $\mathbf{5_b}$. Thus, the Hammett plot shows a large negative slope, −220 ppm, as compared with +5.4 ppm in $[Fe(OETArP)(HIm)_2]^+$. The results suggest that the spin density of the β-carbons gradually increases while that of the *meso*-carbons drastically decreases with the increase in Hammett σ value of the *meso*-phenyl substituents. If the $d_{xy}-a_{1u}$-type interaction is predominant in these complexes, we can expect that the isotropic shifts of the *meso*-carbons should exhibit little substituent dependence since the a_{1u} orbital has a zero coefficient at the *meso*-carbon positions. Furthermore, the $d_{xy}-a_{1u}$-type interaction should induce a large upfield shift of the meso signal relative to that of the corresponding diamagnetic complex. However, even the complex with electron-withdrawing groups such as **3b** has exhibited the meso signal at 280 ppm, which is by ca. 160 ppm more downfield than that of the diamagnetic complex. Thus, we have concluded that *the major interaction in* $[Fe(OETArP)(^tBuNC)_2]^+$ *occurs between the half-filled* d_{xy} *and filled* a_{2u}*-like orbitals, not between the* d_{xy} *and* a_{1u}*-like orbitals*.

It is noteworthy that the isotropic shift of the C_α signal changes from −20 to −40 ppm on going from $\mathbf{1_b}$ to $\mathbf{5_b}$, which clearly indicates that the spin density at the β-pyrrole positions gradually increases with an increase in the Hammett σ value. This is because the electron-withdrawing substituent at the *meso*-phenyl group lowers the energy level of the a_{2u}-like orbital, weakens the $d_{xy}-a_{2u}$ interaction, and consequently stabilizes the d_{xy} orbital relative to the d_π orbitals. This is most explicitly demonstrated in the energy gap diagram in Figure 8 calculated on the basis of the EPR g values. The tetragonality parameter, $|\Delta/\lambda|$, tends to decrease on going from $\mathbf{1_b}$ to $\mathbf{4_b}$; these paramaters are 8.05, 6.93, 7.00, and 2.53, respectively. In the case of $\mathbf{5_b}$, the energy levels of the d_{xy} and d_π orbitals have been reversed, as revealed by the rhombic EPR spectrum. Small energy gap between the d_{xy} and d_π orbitals can also be seen from the curvatures in the Curie plots of these complexes as shown in Figure 4B, which should be ascribed to the contribution from the thermally accessible excited state.[3] As shown in Figure S9 (Supporting Information), DFT calculation of a series of analogous Zn(OETArP) complexes ($\mathbf{1_{Zn}}-\mathbf{4_{Zn}}$) has also indicated the stabilization of the a_{2u}-like orbital due to the electron-withdrawing groups at the phenyl ring; the energy levels of the a_{2u}-like HOMO are −4.05, −4.23, and −4.68 eV for $\mathbf{1_{Zn}}-\mathbf{3_{Zn}}$, respectively. Obviously, there are some discrepancies in the relationship between the $|\Delta/\lambda|$ values and the HOMO energy levels in $\mathbf{3_{Zn}}$ and $\mathbf{4_{Zn}}$. While the $|\Delta/\lambda|$ value in $\mathbf{4_b}$ is much smaller than that in $\mathbf{3_b}$, the HOMO energy level of $\mathbf{4_{Zn}}$ is higher than that of $\mathbf{3_{Zn}}$.

As we have pointed out in a previous paper, some low-spin complexes such as $[Fe(TArP)(CN)_2]^-$ exhibit two types of EPR signals, i.e., axial and large g_{max}-type signals, in solution at extremely low temperatures.[5,53] We have explained the result in terms of the existence of two isomeric complexes adopting different electron configurations; one is a ruffled complex with the $(d_{xz}, d_{yz})^4(d_{xy})^1$ electron configuration and the other is a planar complex with the $(d_{xy})^2(d_{xz}, d_{yz})^3$ electron configuration as shown in eq 1.[5,53] The interconversion of the two isomers is fast on the NMR

$$(d_{xz}, d_{yz})^4(d_{xy})^1 \rightleftarrows (d_{xy})^2(d_{xz}, d_{yz})^3 \quad (1)$$

$$\delta_{obs} = p_{xy}\delta_{xy} + p_\pi\delta_\pi \quad (2)$$

time scale above 173 K where the NMR spectra are taken, while it is slow on the EPR time scale at 4.2 K where the EPR spectra are taken. During the preparation of this paper, a paper written by Scheidt et al. has appeared, expressing a different explanation for the presence of two types of EPR signals.[54,55] On going from $\mathbf{1_b}$ to $\mathbf{4_b}$, the population of the isomer with the $(d_{xy})^2(d_{xz}, d_{yz})^3$ ground state should increase. The observed chemical shifts of the ^1H and ^{13}C signals in low-spin complexes can then be expressed by eq 2 where p_{xy} and p_π are the populations and δ_{xy} and δ_π are the chemical shifts of the isomers with the $(d_{xz}, d_{yz})^4(d_{xy})^1$ and $(d_{xy})^2(d_{xz}, d_{yz})^3$ ground state, respectively. Since the C_α and *meso* signals of the $(d_{xz}, d_{yz})^4(d_{xy})^1$ isomer appear more downfield than those of the $(d_{xy})^2(d_{xz}, d_{yz})^3$ isomer, the increase in population of the $(d_{xy})^2(d_{xz}, d_{yz})^3$ isomer results in the upfield shift of these signals.

Interestingly, the isotropic shift of C_α in $\mathbf{4_b}$ is rather close to that of $\mathbf{4_a}$, though the electronic ground states of these complexes are different; $\delta_{iso} = -41$ and −47 ppm for $\mathbf{4_b}$ and $\mathbf{4_a}$, respectively. This does not necessarily mean that the population of the $(d_{xy})^2(d_{xz}, d_{yz})^3$ isomer in $\mathbf{4_b}$ is close to that of $\mathbf{4_a}$. The result should rather be explained in terms of the effective spin delocalization in the $(d_{xy})^2(d_{xz}, d_{yz})^3$ isomer of the bis(^{t}BuNC) complex as compared with that of the bis(HIm) complex. The interaction between the d_π and $4e_g$*-like orbitals could also be considered since the $4e_g$*-like orbital is stabilized due to the presence of electron-withdrawing aryl groups at the meso positions as deduced from the energy-level diagrams of analogous Zn(OETArP). As mentioned, we have recently reported that $[Fe(DAzP)(^tBuNC)_2]^+$,

(53) Ikezaki, A.; Nakamura, M. *Inorg. Chem.* **2002**, *41*, 2761−2768.
(54) Regarding eq 1 in our previous paper,[53] Scheidt et al. described that the interconversion of two conformers on the EPR timescale is not necessary and even unlikely, given the low temperature of the measurement.[55] In the previous paper, we have described that the mutual exchange between the two species in eq 1 is slow on the EPR timescale, which indicates that the rate constant for interconversion is much smaller than 10^9 s^{-1}; it could be 10^{-5} s^{-1} or less.
(55) Li, J.; Noll, B. C.; Schulz, C. E.; Scheidt, W. R. *Inorg. Chem.* **2007**, *46*, 2286−2298.

which adopts the $(d_{xy})^2(d_{xz}, d_{yz})^3$ ground state at ambient temperature despite the coordination of ^{t}BuNC, shows an effective spin delocalization to the macrocycle as compared with $[Fe(DAzP)(DMAP)_2]^+$, although the latter complex also adopts the $(d_{xy})^2(d_{xz}, d_{yz})^3$ ground state.[52] The chemical shifts of the α-CH_2 signals of the butyl groups are −35.4 and −21.8 ppm for the bis(^{t}BuNC) and bis(DMAP) complexes, respectively. Correspondingly, the spin densities at the pyrrole β carbon atoms are determined to be 0.016 and 0.011 in the former complex as compared with 0.010 and 0.0094 in the latter one. Another example showing the effective spin delocalization in the bis(^{t}BuNC) complex was $[Fe(OEC)(^t\text{BuNC})_2]^+$ reported by Cai et al.[56] This complex is quite unique because the pyrroline-H signal appears at 128.3 ppm while the *meso*-H signals resonate at −71.7 and −43.0 ppm. Extremely large downfield and upfield shifts of the peripheral proton signals have been interpreted in terms of the equilibrium between planar complex with the $(d_{xy})^2(d_{xz}, d_{yz})^3$ ground state and the ruffled complex with the $(d_{xz}, d_{yz})^4(d_{xy})^1$ ground state; the $(d_{xz}, d_{yz})^4(d_{xy})^1$ isomer shifts the *meso*-H signal to the upfield positions while the $(d_{xy})^2(d_{xz}, d_{yz})^3$ isomer induces the downfield shift of the pyrroline-H signal. Since the chemical shift of the pyrroline-H signal in $[Fe(OEC)(HIm)_2]^+$, which is a typical complex with the $(d_{xy})^2(d_{xz}, d_{yz})^3$ ground state, is 12.0 ppm, the large downfield shift in $[Fe(OEC)(^t\text{BuNC})_2]^+$ is a direct indication that the spin delocalization from the metal d_π to the porphyrin p_π orbitals is quite effective.

Conclusion

Hammett plots of the isotropic shifts of the CH_2, C_α, and *meso*-C signals in highly saddled low-spin $[Fe(OETArP)(HIm)_2]^+$ (**1**$_a$−**5**$_a$) and $[Fe(OETArP)(^t\text{BuNC})_2]^+$(**1**$_b$−**5**$_b$), where Ar represents substituted *meso*-phenyl groups, have been examined to reveal if the symmetry-allowed interaction between iron d_{xy} and porphyrin a_{1u}-like orbitals is strong enough to affect the chemical shifts of the complexes. EPR spectra have revealed that all the bis(HIm) complexes examined in this study adopt the $(d_{xz}, d_{yz})^3(d_{xy})^2$ ground state. These complexes have exhibited a fairly small substituent effect on the chemical shifts because the half-occupied d_π orbitals carrying unpaired electrons interact with the porphyrin $3e_g$-like orbitals having a zero coefficient at the *meso*-carbon positions. In the case of the bis(^{t}BuNC) complexes, the EPR spectra have revealed that all the complexes except **5**$_b$ adopt the $(d_{xz}, d_{yz})^4(d_{xy})^1$ ground state; **5**$_b$ is actually the first iron(III) porphyrinate that shows the $(d_{xz}, d_{yz})^3(d_{xy})^2$ ground state despite the coordination of ^{t}BuNC. The chemical shifts of these complexes have shown a large substituent dependence as compared with those of bis(HIm) complexes. The slopes of Hammett plots for the *meso*-C isotropic shifts are −220 and +5.4 ppm for bis(^{t}BuNC) and bis(HIm) complexes, respectively. If the half-occupied d_{xy} orbital in bis(^{t}BuNC) complexes interacts with the a_{1u}-like orbital, we can expect a large upfield shift of the *meso*-C signal together with a negligibly small substituent effect because the a_{1u} orbital has a zero coefficient at the *meso*-carbons and a relatively large coefficient at the pyrrole α-carbons in D_{4h} iron(III) porphyrinates. Thus, we have concluded that the half-occupied d_{xy} orbitals in low-spin saddle-shaped bis(^{t}BuNC) complexes interact mainly with the a_{2u}-like orbital; the interaction with the a_{1u}-like orbital should be negligibly small, though the $d_{xy}-a_{1u}$ interaction is symmetry-allowed in saddle-shaped complexes. Smaller spin delocalization to the *meso*-carbon atoms in the complexes with electron-withdrawing groups such as **3**$_b$ and **4**$_b$ is then ascribed to the decrease in spin population in the d_{xy} orbital due to a smaller energy gap between the d_{xy} and d_π orbitals. In fact, the energy levels of the d_{xy} and d_π orbitals are completely reversed in **5**$_b$, which has strongly electron-withdrawing CF_3 groups at the 3- and 5-positions of the *meso*-phenyl group. It should be emphasized here that a negligibly small interaction between half-occupied d_{xy} and porphyrin a_{1u}-like orbitals in saddle-shaped low-spin ($S = {}^1/_2$) iron(III) porphyrinates does not necessarily rule out the possibility of strong $d_{xy}-a_{1u}$ interaction in the corresponding intermediate-spin ($S = {}^3/_2$) $[Fe(OETPP)(THF)_2]^+$ complex as proposed by Cheng and co-workers on the basis of the theoretical calculation.[24] Furthermore, Rivera and co-workers have reported that a heme-containing enzyme should adopt the $S = {}^3/_2$, $(d_{xz})^3(d_{yz})^1(d_z{}^2)^1$ electron configuration on the basis of the ^{13}C NMR data.[57] We are now applying a similar methodology to a series of intermediate-spin $[Fe(OETArP)(THF)_2]^+$ complexes to reveal the nature of the metal−porphyrin orbital interactions in the intermediate-spin complexes.

Experimental Section

Spectral Measurements. UV−vis spectra were measured on a Shimadzu MultiSpec-1500 spectrophotometer at ambient temperature. Fast atom bombardment mass spectrometry (FAB-MS) spectra were measured on a JEOL JMS-600H device using 3-nitrobenzyl alcohol as the matrix. ^{1}H and ^{13}C NMR spectra were recorded on a JEOL LA300 spectrometer operating at 300.4 MHz for ^{1}H. Chemical shifts were referenced to the residual peak of dichloromethane ($\delta = 5.32$ ppm for ^{1}H and 53.8 ppm for ^{13}C). EPR spectra were measured at 4.2−20 K with a Bruker E500 or Bruker EMX plus spectrometer operating at the X band and equipped with an Oxford helium cryostat. The concentrations of EPR samples were 5−8 mM. The *g* values were estimated by the simulation of the observed spectra.

Synthesis. 1. Zn(OETArP). Free base porphyrins, H_2(OETArP), where Ar is substituted phenyls, were prepared by the condensation reactions between 3,4-diethylpyrrole and substituted benzaldehydes according to the literature.[58,59] The free base porphyrins were converted to the corresponding zinc complexes Zn(OETArP) for the characterization. The ^{1}H and ^{13}C NMR chemical shifts of these complexes are listed in Tables 4 and 6. UV−vis spectra (CH_2Cl_2, λ_{max} nm) and FAB-MS: **1**$_{Zn}$, 457, 588, 646 nm; $m/e = 1020$ (M^+).

(56) Cai, S.; Lichtenberger, D. L.; Walker, F. A. *Inorg. Chem.* **2005**, *44*, 1890−1903.

(57) Zeng, Y.; Caignan, G. A.; Bunce, R. A.; Rodriguez, J. C.; Wilks, A.; Rivera, M. *J. Am. Chem. Soc.* **2005**, *127*, 9794−9807.

(58) Evans, B.; Smith, K. M.; Fuhrhop, J.-H. *Tetrahedron Lett.* **1977**, *18*, 443−446.

(59) Barkigia, K. M.; Berber, M. D.; Fajer, J.; Medforth, C. J.; Renner, M. W.; Smith, K. M. *J. Am. Chem. Soc.* **1990**, *112*, 8851−8857.

$\mathbf{3_{Zn}}$, 459, 592, 648 nm; m/e = 1172 (M^+), 1144 ($M^+ - 28$). $\mathbf{4_{Zn}}$, 468, 601 nm; m/e = 1172 (M^+). $\mathbf{5_{Zn}}$, 458, 588, 674 nm; m/e = 1416 ($M^+ - 28$).

2. Fe(OETArP)Cl. The insertion of iron to H_2(OETArP) was carried out using $FeCl_2 \cdot 4H_2O$ in refluxing $CHCl_3-CH_3OH$ (3:1) solution under argon atmosphere.[21,60] The reaction mixture was treated with diluted HCl solution. The organic layer was separated and dried over sodium sulfate. Evaporation of the solvents yielded a dark brown solid, which was purified by chromatography on silica gel using $CH_2Cl_2-CH_3OH$ as eluents. ^{1}H NMR(CD_2Cl_2, 298 K, δ ppm). *Ar = 4-OMePh*: 45.3 (4H, CH_2); 37.7 (4H, CH_2); 34.6 (4H, CH_2); 23.0 (4H, CH_2); 3.58 (12H, CH_3); 1.41 (12H, CH_3); 11.11 (*o*-H, 4H); 8.54 (*o*-H, 4H); 12.50 (*m*-H, 4H); 12.27 (*m*-H, 4H); 5.52 (*p*-OCH_3, 12H). *Ar = Ph*: 46.0 (4H, CH_2); 38.3 (4H, CH_2); 35.4 (4H, CH_2); 23.8 (4H, CH_2); 3.65 (12H, CH_3); 1.87 (12H, CH_3); 10.57 (*o*-H, 4H); 8.15 (*o*-H, 4H); 13.00 (*m*-H, 4H); 12.87 (*m*-H, 4H); 7.1 (*p*-H, 4H). *Ar = 4-CF_3-Ph*: 46.1 (4H, CH_2); 41.3 (4H, CH_2); 36.5 (4H, CH_2); 26.1 (4H, CH_2); 4.23 (12H, CH_3); 1.75 (12H, CH_3); 10.27 (*o*-H, 4H); 7.87 (*o*-H, 4H); 13.63 (*m*-H, 4H); 13.54 (*m*-H, 4H). *Ar = 3,5-$(CF_3)_2$-Ph*: 45.9 (4H, CH_2); 43.4 (4H, CH_2); 38.0 (4H, CH_2); 28.5 (4H, CH_2); 4.69(12H, CH_3); 2.27(12H, CH_3); 10.21(*o*-H, 4H); 7.95 (*o*-H, 4H); 7.19 (*p*-H, 4H). *Ar = 2,6-Cl_2-Ph*: 43.4 (4H, CH_2); 39.4 (4H, CH_2); 35.3 (4H, CH_2); 25.1 (4H, CH_2); 4.18 (12H, CH_3); 2.45 (12H, CH_2); 13.42 (*m*-H, 4H); 13.14 (*m*-H, 4H); 7.70 (*p*-H, 4H).

3. [Fe(OETArP)(HIm)$_2$]Cl ($\mathbf{1_a}-\mathbf{5_a}$). To a CD_2Cl_2 solution of Fe(OETArP)Cl placed in an NMR sample tube was added 4−6 equiv of imidazole. The ^{1}H NMR spectrum of the sample thus formed clearly showed the formation of low-spin bis(imidazole) complexes ($\mathbf{1_a}-\mathbf{5_a}$). The ^{1}H and ^{13}C NMR chemical shifts are listed in Tables 4 and 6, respectively. Samples for EPR measurements were similarly prepared by the addition of 6−10 equiv of imidazole into a CH_2Cl_2 solution of Fe(OETArP)Cl. The g values are given in Table 6.

4. [Fe(OETArP)(^{t}BuNC)$_2$]Cl ($\mathbf{1_b}-\mathbf{5_b}$). These complexes were obtained by the addition of 4−6 equiv of ^{t}BuNC to a CD_2Cl_2 solution of [Fe(OETArP)(THF)$_2$]ClO_4; the latter complexes were prepared by the addition of $AgClO_4$ to Fe(OETArP)Cl in THF solution. The ^{1}H and ^{13}C NMR chemical shifts are listed in Tables 4 and 6, respectively. Samples for EPR were similarly prepared by the addition of 6−10 equiv of ^{t}BuNC into a CH_2Cl_2 solution of [Fe(OETArP)(THF)$_2$]ClO_4. The g values are given in Table 6.

X-ray Crystallographic Analysis. 1. Preparation of Crystals and Experimental Details. [Fe(OETArP)(HIm)$_2$]$ClO_4 \cdot CH_2Cl_2$-($\mathbf{1_a}$); Ar = 4-OMePh. The purple solid of bis(THF) complex, [Fe(OETArP)(THF)$_2$]ClO_4, Ar = 4-OMePh, was dissolved in a CH_2Cl_2/heptane solution containing 4−10 equiv of imidazole, and the solution was allowed to stand at room temperature. A purple platelet crystal with dimensions of 0.51 × 0.40 × 0.12 mm thus obtained was used for the diffraction experiment. Crystal data and experimental and refinement details for crystal structure determination are summarized in Table 1. The asymmetric unit contains one porphyrin, one perchlorate counterion, and one dichloromethane as crystal solvent. All non-hydrogen atoms were refined anisotropically.

[Fe(OETArP)(HIm)$_2$]Cl$\cdot$(C_6H_{12})$_{0.5}\cdot$($CHCl_3$)$_4$ ($\mathbf{2_a}$); Ar = Ph. The purple solid of the chloride complex, Fe(OETPP)Cl, was dissolved in a $CHCl_3$/cyclohexane solution containing 4−10 equiv of imidazole, and the solution was allowed to stand at room temperature. A purple prismatic crystal with dimensions of 0.2 × 0.1 × 0.1 mm thus obtained was used for the diffraction experiment. Crystal data and experimental and refinement details for crystal structure determination are summarized in Table 1. The asymmetric unit contains one porphyrin, one chloride counterion, four chloroform molecules as crystal solvent, and a half molecule of cyclohexane on the center of symmetry. The distances and angles in the cyclohexane molecule were fixed to idealized values. Two of the four chloroform molecules were highly disordered to have two or three sites in the structure. The site occupancy for each chloroform molecule was refined to be 0.65(1)/0.35(1) and refined and fixed to be 0.44/0.40/0.16. One of the ethyl groups at the Py-β position was also disordered over two positions with population of 0.57-(2)/0.43(2). The second-extinction effect was corrected by the *SHELXL* method. The extinction coefficient was refined to be 0.016(2).

[Fe(OETArP)(HIm)$_2$]$ClO_4 \cdot CH_2Cl_2$($\mathbf{3_a}$); Ar = 4-CF_3Ph. The purple solid of the bis(THF) complex, [Fe(OETArP)(THF)$_2$]ClO_4, Ar = 4-CF_3Ph, was dissolved in a CH_2Cl_2/heptane solution containing 4−10 equiv of imidazole, and the solution was allowed to stand at room temperature. A purple platelet crystal with dimensions of 0.2 × 0.2 × 0.1 mm thus obtained was used for the diffraction experiment. The TWIN refinement was applied (Flack χ parameter = 0.400). The asymmetric unit contains one porphyrin, one perchlorate counterion, and one dichloromethane as crystal solvent. The second-extinction effect was corrected by the *SHELXL* method, and the coefficient was refined to be 0.007(1). All non-hydrogen atoms were refined anisotropically.

[Fe(OETArP)(HIm)$_2$]$ClO_4 \cdot$(C_6H_6)$_{0.5}$(CH_2Cl_2) ($\mathbf{4_a}$); Ar = 2,6-Cl_2Ph. The purple solid of the bis(THF) complex, [Fe(2,6-Cl_2-OETPP)(THF)$_2$]ClO_4, was dissolved in a CH_2Cl_2/benzene/heptane solution containing 4−10 equiv of imidazole, and the solution was allowed to stand at room temperature. A purple platelet crystal with dimensions of 0.2 × 0.2 × 0.1 mm thus obtained was used for the diffraction experiment. The asymmetric unit contains one porphyrin, one perchlorate counterion, one dichloromethane as crystal solvent, and a half of a benzene molecule on the center of symmetry. The distances and angles in the benzene molecule were fixed to idealized values. One of the ethyl groups at the Py-β position is also disordered over two positions with population of 0.56(1)/0.44(1). Non-hydrogen atoms except for the benzene molecule were refined anisotropically.

2. Data Collection. The diffraction data of **1a** were collected at 90 K on a Rigaku AFC-8 diffractometer equipped with a Saturn 70 CCD area detector with focused and monochromated Mo Kα radiation (λ = 0.71073 Å) by a confocal mirror and a rotating anode generator. The data were collected to a maximum 2θ value of 65.1°. A total of 1980 images was collected with three different goniometer settings, and the total oscillation angle of each setting is 330° corresponding to 660 images, for **1a**. The exposure time was 1 s per degree in ω. The crystal-to-detector distance was 40.09 mm. The readout was performed in the 0.285714 mm pixel mode. Data were processed by the *CrystalClear SM* program package.[53] A numerical absorption correction was applied.

Diffraction data of $\mathbf{2_a}$, $\mathbf{3_a}$, and $\mathbf{5_a}$ were collected at 298 K on a Rigaku RAXIS-RAPID Imaging Plate diffractometer with graphite monochromated Mo Kα radiation (λ = 0.71073 Å) and a rotating anode generator. The indexing was performed from three oscillations, which were exposed for 0.8 min for $\mathbf{3_a}$ and $\mathbf{5_a}$ and for 2.5 min for $\mathbf{2_a}$. The data were collected at 298 K to a maximum 2θ value of 55°. A total of 86, 78, and 192 images, corresponding to the 388.5°, 390.0°, and 384° oscillation angles, was collected with three different goniometer settings for $\mathbf{2_a}$, $\mathbf{3_a}$, and $\mathbf{5_a}$, respectively.

(60) Sparks, L. D.; Medforth, C. J.; Park, M.-S.; Chamberlain, J. R.; Ondrias, M. R.; Senge, M. O.; Smith, K. M.; Shelnutt, J. A. *J. Am. Chem. Soc.* **1993**, *115*, 581−592.

The exposure time was 2.00 min per degree for $\mathbf{2_a}$ and 1.00 min per degree for $\mathbf{3_a}$ and $\mathbf{5_a}$. The camera radius was 127.40 mm. The readout was performed in the 0.100 mm pixel mode. Data were processed by the *PROCESS-AUTO* program package. A symmetry-related absorption correction was carried out by using the program *ABSCOR*.[62]

3. Structure Solution and Refinement. The structures were solved by direct methods with the program *SIR2004*.[63] The structure refinement was carried out by the full-matrix least-squares refinement with *SHELXL-97*.[64] All the hydrogen atoms were calculated. The positional parameters of the H atoms were constrained to have C−H distances of 0.96 Å for primary, 0.97 Å for secondary, and 0.93 Å for aromatic H atoms. The H-atom *U* values were constrained to have 1.2 times the equivalent isotropic *U* values of their attached atoms (1.5 for methyl groups). The atomic scattering factors were taken from the International Tables for Crystallography. Crystallographic data (excluding structure factors) for the structures reported in this paper have been deposited with the Cambridge Crystallographic Data Centre as supplementary publication Nos. CCDC-635316−635319. Copies of the data can be obtained free of charge on application to the CCDC, 12 Union Road, Cambridge CB2 1EZ, U.K. (fax: (+44) 1223 336−033; e-mail: deposit@ccdc.cam.ac.uk).

Computational Details. DFT calculations of a series of Zn(OETArP) complexes were carried out using the *Scigress Explorer DFT*, version 7, program.[65] The geometries of the corresponding $[Fe(OETArP)(HIm)_2]^+$ complexes determined by X-ray crystallography were used for the calculation. All the frontier orbitals together with the corresponding energy levels were calculated with the generalized gradient approximation (GGA) of B88−PW91[66−69] and a double-ζ valence polarization (DZVP) basis set.[70]

Acknowledgment. This work was supported by Research Promotion Grants from the Toho University Graduate School of Medicine (Nos. 05-21 and 06-01 to Y.O.) and by Grant-in-Aid for Scientific Research from the Ministry of Education, Culture, Sports, Science and Technology, Japan (No. 18655025 to Y.O. and No. 16550061 to M.N.). This work was also supported by the Research Center for Materials with Integrated Properties, Toho University. We also thank the the Research Center for Molecular-Scale Nanoscience and the Institute for Molecular Science (IMS).

Supporting Information Available: Figures S1−S4, respective packing diagrams of $\mathbf{1_a}$−$\mathbf{4_a}$; Figure S5, ORTEP diagrams of $\mathbf{2_a}$; Figure S6, ORTEP diagrams of $\mathbf{3_a}$; Figure S7, ORTEP diagrams of $\mathbf{4_a}$; Figure S8, simulation of the observed EPR spectra; Figure S9, energy levels of porphyrin π orbitals in Zn(OETArP) ($\mathbf{1_{Zn}}$−$\mathbf{4_{Zn}}$) determined by DFT calculation. This material is available free of charge via the Internet at http://pubs.acs.org.

IC700827W

(61) *CrystalClear SM* program package; Rigaku Corp., Tokyo, Japan, 1999. *CrystalClear Software User's Guide*; Molecular Structure Corp., Tokyo, Japan, 2000. Pflugrath, J. W. *Acta Crystallogr*. **1999**, *D55*, 1718−1725.
(62) Higashi, T. *Program for Absorption Correction*; Rigaku Corp.: Tokyo, Japan, 1995.
(63) *SIR 2004*: Burla, M. C.; Caliandro, R.; Camalli, M.; Carrozzini, B.; Cascarano, G. L.; De Caro, L.; Giacovazzo, C.; Polidori, G.; Spagna, R. *J. Appl. Crystallogr*. **2005**, *38*, 381−388.
(64) Sheldrick, G. M. *SHELXL97, Program for the Refinement of Crystal Structures*; University of Göttingen: Göttingen, Germany, 1997.
(65) *Scigress Explorer DFT*, version 7; Fujitsu, Ltd.: Tokyo, Japan, 2007.
(66) Becke, A. D. *Phys. Rev. A*: *At., Mol., Opt. Phys*. **1988**, *38*, 3098−3100.
(67) Becke, A. D. *J. Chem. Phys.* **1988**, *88*, 2547−2553.
(68) Perdew, J. P. In *Electronic Properties of Solids '91*; Ziesche, P., Eschrig, H., Eds.; Akademie Verlag: Berlin, 1991.
(69) Perdew, J. P.; Chevary, J. A.; Vosko, S. H.; Jackson, K. A.; Pederson, M. R.; Singh, D. J., *Phys. Rev. B: Condens. Matter Mater. Phys.* **1992**, *46*, 6671−6687.
(70) Godbout, N.; Salahub, D. R.; Andzelm, J.; Wimmer, E. *Can. J. Chem.* **1992**, *70*, 560−571.